

Samuel Potter

Department of Mechanical Engineering,
Willerson Center for Cardiovascular
Modeling and Simulation,
Institute for Computational Engineering
and Sciences,
The University of Texas at Austin,
240 East 24th Street,
Austin, TX 78712

Jordan Graves

Department of Biomedical Engineering,
Willerson Center for Cardiovascular
Modeling and Simulation,
Institute for Computational Engineering
and Sciences,
The University of Texas at Austin,
240 East 24th Street,
Austin, TX 78712

Borys Drach

Department of Mechanical and
Aerospace Engineering,
New Mexico State University,
Las Cruces, NM 88003

Thomas Leahy

Department of Biomedical Engineering,
Willerson Center for Cardiovascular
Modeling and Simulation,
Institute for Computational Engineering and Sciences,
The University of Texas at Austin,
240 East 24th Street,
Austin, TX 78712

Chris Hammel

Department of Mechanical Engineering,
Willerson Center for Cardiovascular
Modeling and Simulation,
Institute for Computational Engineering and Sciences,
The University of Texas at Austin,
240 East 24th Street,
Austin, TX 78712

Yuan Feng

Center for Molecular Imaging and Nuclear Medicine,
School of Radiological and Interdisciplinary
Sciences (RAD-X),
Soochow University,
Collaborative Innovation Center of Radiation
Medicine of Jiangsu Higher Education Institutions,
Suzhou 215123, China

Aaron Baker

Department of Biomedical Engineering,
Willerson Center for Cardiovascular
Modeling and Simulation,
The University of Texas at Austin,
107 W Dean Keeton Street, Stop C0800,
Austin, TX 78712

Michael S. Sacks¹

Department of Biomedical Engineering,
Willerson Center for Cardiovascular Modeling and
Simulation,
Institute for Computational Engineering and Sciences,
The University of Texas at Austin,
240 East 24th Street,
Austin, TX 78712

A Novel Small-Specimen Planar Biaxial Testing System With Full In-Plane Deformation Control

Simulations of soft tissues require accurate and robust constitutive models, whose form is derived from carefully designed experimental studies. For such investigations of membranes or thin specimens, planar biaxial systems have been used extensively. Yet, all such systems remain limited in their ability to: (1) fully prescribe in-plane deformation gradient tensor \mathbf{F}_{2D} , (2) ensure homogeneity of the applied deformation, and (3) be able to accommodate sufficiently small specimens to ensure a reasonable degree of material homogeneity. To address these issues, we have developed a novel planar biaxial testing device that overcomes these difficulties and is capable of full control of the in-plane deformation gradient tensor \mathbf{F}_{2D} and of testing specimens as small as $\sim 4\text{ mm} \times \sim 4\text{ mm}$. Individual actuation of the specimen attachment points, combined with a robust real-time feedback control, enabled the device to enforce any arbitrary \mathbf{F}_{2D} with a high degree of accuracy and homogeneity. Results from extensive device validation trials and example tissues illustrated the ability of the device to perform as designed and gather data needed for developing and validating constitutive models. Examples included the murine aortic tissues, allowing for investigators to take advantage of the genetic manipulation of murine disease models. These capabilities highlight the potential of the device to serve as a platform for informing and verifying the results of inverse models and for conducting robust, controlled investigation into the biomechanics of very local behaviors of soft tissues and membrane biomaterials. [DOI: 10.1115/1.4038779]

Keywords: mechanical, testing, devices

¹Corresponding author.

Manuscript received June 1, 2017; final manuscript received December 11, 2017; published online February 13, 2018. Assoc. Editor: Thao (Vicky) Nguyen.

1 Introduction

There continues to exist many pathophysiological and biomedical device applications where robust mathematical models of soft biological materials are required. Under the framework of pseudo-hyperelasticity [1], experimentation involving all relevant deformations is necessary to determine the form of a strain-energy density function Ψ . The anisotropic, nonlinear mechanical behavior of this class of biological tissues and similarly behaving biomaterials makes data derived from uniaxial testing insufficient, so that multi-axial test data are necessary [2]. In biomembrane applications, planar biaxial testing is the desired testing modality from which the stress and strain tensors can be determined directly from experimental data [3]. Many devices exist that accomplish these objectives for extensional loading scenarios [4] and for applying in-plane shear [5].

In addition to determining the Ψ form, validation of inverse models has become increasingly relevant in many biomechanics applications for both in vitro [6,7] and in vivo problems [8]. Inverse models, which utilize in vivo measures of tissue behavior, represent an exciting tool for determining local tissue behaviors without the invasive nature and complications inherent in excised tissue testing [7]. However, inverse models must be verified against experimental data; uniquely challenging because they are developed from measures of large tissue sections or even complete organs, yet must be verified on a regional basis to ensure local behaviors are faithfully captured. Thus, a planar biaxial testing device must be able to test small specimens, typically in the range of 3–5 mm. This size range also enables the opportunity to test tissues from murine models and leverage the genetically and biochemically tunable platform they provide for testing vascular tissues [9]. Moreover, the form of the Ψ must be assumed a priori.

Beyond the above considerations, planar tissue testing approaches must be able to fully control the in-plane deformation gradient tensor \mathbf{F}_{2D} . This enables precise application of any relevant loading path required, including both extensional and shear alone or in combination. Moreover, homogeneity of the prescribed \mathbf{F}_{2D} within a known subregion is important to ensure that the extracted stress and strain data accurately represents the local tissue behaviors. Any induced heterogeneities will introduce errors, as the resulting stress and strain data will be but an average of the actual local values. While some success applying in-plane shear has been achieved [5], these approaches were contingent on a priori knowledge of the specimen's material axes. Such information may not always be available and it may be intractable to obtain prior to testing. More importantly, the shear obtained in the above mentioned study was not controllable, i.e., it was a function of the specimen's particular mechanical properties and as such could not be predicted or prescribed. To date, no device yet exists that possesses the above mentioned capabilities.

Toward this end, we have developed a new biaxial testing system that is able to: (1) independently control the four components of \mathbf{F}_{2D} in a homogeneously deforming region in the center of the test specimen and (2) test relatively small specimens (~4 mm per side). The data that this device can provide will be instrumental in the verification and further development of constitutive models of biological tissues, including inverse models.

2 Methods

2.1 Design Objectives. In order to meet the needs described above, specific design objectives were defined for the present device as follows:

- (1) Determination of in-plane stress tensor directly from measured quantities.
- (2) Real-time, feedback based control of complete in-plane deformation gradient tensor.
- (3) Homogeneous deformation within central third of specimen control region. The central third region was selected based

on previous studies [10–12] indicating it would be largely free of boundary effects.

- (4) Direct attachment system without clamps for simple boundary conditions.
- (5) Capable of testing planar specimens of tissue in a size range of 4 mm × 4 mm. This size range accommodates testing murine tissue models and regional investigation of larger tissues.

2.1.1 Kinematics of a Biaxial Test. Let \mathbf{X} represent three-dimensional positions of material particles within a body with an initial configuration, and \mathbf{x} represent the position of the material particles in that body at some deformed configuration. The deformation gradient tensor is defined as $\mathbf{x} = \mathbf{F}\mathbf{X}$, where $\mathbf{F} = \nabla \mathbf{x}$. For a general three-dimensional deformation, \mathbf{F} can be written as

$$\mathbf{F} = \begin{bmatrix} \frac{\partial \mathbf{x}_1}{\partial \mathbf{X}_1} & \frac{\partial \mathbf{x}_1}{\partial \mathbf{X}_2} & \frac{\partial \mathbf{x}_1}{\partial \mathbf{X}_3} \\ \frac{\partial \mathbf{x}_2}{\partial \mathbf{X}_1} & \frac{\partial \mathbf{x}_2}{\partial \mathbf{X}_2} & \frac{\partial \mathbf{x}_2}{\partial \mathbf{X}_3} \\ \frac{\partial \mathbf{x}_3}{\partial \mathbf{X}_1} & \frac{\partial \mathbf{x}_3}{\partial \mathbf{X}_2} & \frac{\partial \mathbf{x}_3}{\partial \mathbf{X}_3} \end{bmatrix} = \begin{bmatrix} \lambda_1 & \kappa_{12} & \kappa_{13} \\ \kappa_{21} & \lambda_2 & \kappa_{23} \\ \kappa_{31} & \kappa_{32} & \lambda_3 \end{bmatrix} \quad (1)$$

where λ_i are axial stretch ratios and κ_{ij} describe the shear. For planar biaxial testing, $\kappa_{31}, \kappa_{13}, \kappa_{23}, \kappa_{32} = 0$ [13]. We further simplify the notation with $\kappa_{12} = \kappa_1, \kappa_{21} = \kappa_2$ so that a general \mathbf{F} for a biaxial test can then be written as

$$\mathbf{F} = \begin{bmatrix} \lambda_1 & \kappa_1 & 0 \\ \kappa_2 & \lambda_2 & 0 \\ 0 & 0 & \lambda_3 \end{bmatrix} \quad (2)$$

For most biological tissues, incompressibility is assumed [1] so that $\det(\mathbf{F}) = 1 \Rightarrow \lambda_3 = 1/(\lambda_1\lambda_2 - \kappa_2\kappa_1)$. From this, we subcategorize the following common modes of planar biaxial deformation as generalized (G), simple extension (SE), simple shear (S1, S2), and pure shear (S3) (Fig. 1).

2.1.2 Strain and Load Ranges. Reported normal stresses during biaxial tests of biological tissue generally range between 50 kPa and 1 MPa, with associated strains ranging between −3% and 70% [2,14]. Shear stresses range from ±40 kPa, with corresponding κ_1, κ_2 ranging from ±0.1 [5].

2.1.3 In-Plane Deformation Gradient Control. Full control of \mathbf{F} presents several difficulties, including the unknown mechanical response of the specimen, which can be both highly anisotropic and nonlinear. In addition, the device must control \mathbf{F} through linear actuation of point attachments at the specimen boundary, and thus be able to quickly correct for errors in the deformation gradient brought on by the above mentioned material parameter uncertainties. To address these difficulties, we developed a control system robust enough to handle nonlinear coupling and large parameter uncertainty, paired with a feedback system that can track the deformation gradient in real time.

2.1.4 Homogeneity Within the Inner Region. The need for homogeneous stress and strain fields is fundamental to the determination of stress tensors from experimentally measured quantities [3]. More importantly, a homogeneous stress–strain field allows for more precise determination of the mechanical properties of a specimen as it represents the relationship between a single load value and a single deformation value (as opposed to the area averaged deformation value generated from a heterogeneous deformation and stress). As the deformation gradient is intrinsically linked to the strain and stress fields, and is the quantity being prescribed and controlled with this device, the homogeneity requirement is placed on \mathbf{F} . It is worth noting that, in addition to the assumption of homogeneous stress–strain fields in the inner

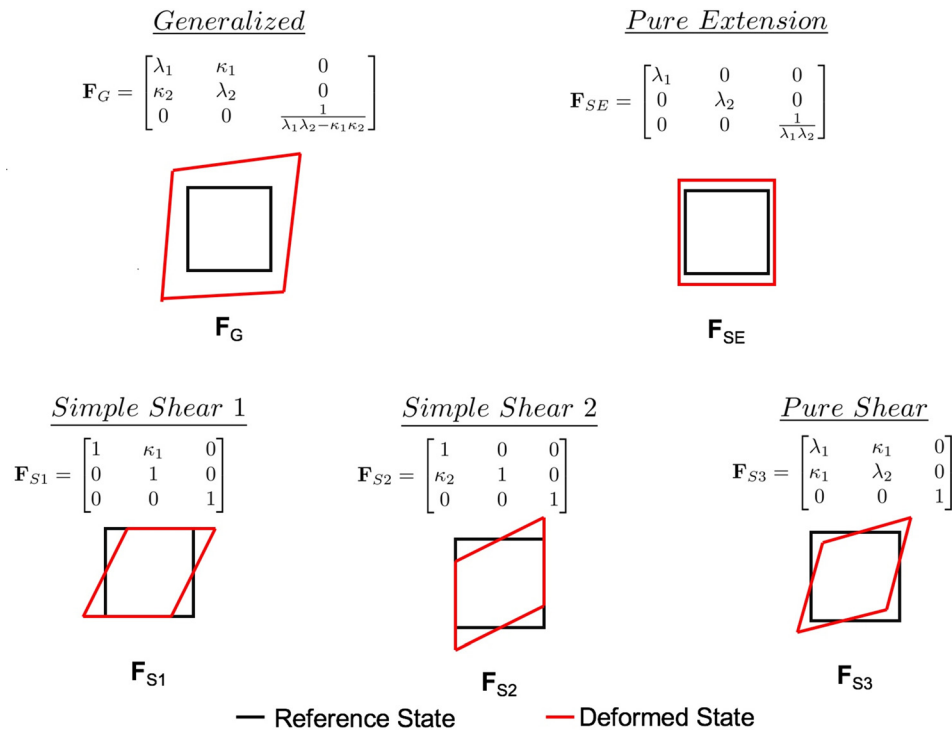


Fig. 1 Common modes of planar biaxial deformation that the device is designed to prescribe and control

region, the accurate determination of a specimen's material properties also assumes that those properties are relatively homogeneous throughout the inner marker region (1 mm × 1 mm). Though biological tissue is inherently nonhomogeneous, the small size of the region on which the homogeneity assumption is placed gives confidence that it is a reasonable one. Several studies have investigated the effects various attachment methods have on the homogeneity of both stress and strain within the inner region of the specimen [12,15,16]. Among the factors studied include specimen geometry and size, gripping technique, apron size (distance between the attachment point and the edge of the specimen), and number and spacing of attachment points [12,15,16]. Except for apron size, all of these factors have been shown to contribute to significant differences in derived stress-strain response [15].

In addition to the factors mentioned above, studies of point-based attachment methods have shown that as specimen size decreases (an inevitable occurrence given the additional objective of small specimen size), small deviations in point spacing from the ideal symmetric, evenly spaced pattern begin to severely impact the distribution of stresses and strains within the inner region [15]. For this reason, it is especially important for a device that the attachment points be placed with precision and consistency. The exact placement of the attachment points should be close enough to the edge to eliminate boundary effects while remaining far enough from the edge to ensure the attachments do not tear through the apron of the specimen. It has also been shown that as the number of attachment points increases, the more homogeneous the stress and strains are in the inner region [15]. However, the scale of the present device places a limit on a practical number of attachments points per side.

2.1.5 Attachment System. The choice of specimen attachment system dictates the boundary conditions. Sun et al. showed that the choice of boundary condition affects the ability to determine stress and strain information directly from experimental data, which is an important objective when developing and validating constitutive laws [12]. Furthermore, Zhang et al. recently

introduced a robust method for determining the stress strain relationship from biaxial test data that accounts for rigid body rotation [3]. This method greatly improves the accuracy of material parameter estimation in cases of high in-plane shear and assumes a tethered boundary condition at the specimen edges [3]. In addition to these factors, the attachment system influences the ease of experiment execution and the ability to directly prescribe either stress or deformation protocols. This range of influence underlines the key importance of the attachment system design. Point-based methods thus continue to be the most common for biological tissue specimens, due to their ability to allow lateral expansion of the specimen edges and to easily transmit boundary loads to the central region of interest [12].

2.1.6 Specimen Size. A number of factors need to be considered to determine practical specimen size limits. For example, murine animals present an ideal platform for investigating the effect of genetic and biochemical factors on the mechanical response of vascular tissues [9]. Typical murine central arteries range in size from 400 to 1000 μm in diameter and 3–5 mm long [9]. Other considerations regarding specimen size include the need for regional investigation of the mechanical response of larger tissue types, e.g., the aortic valve leaflet. Billiar and Sacks showed that the stress-strain response of the aortic valve leaflet varies widely with location [14]. These factors lead to a specimen size range objective of 4 mm × 4 mm, which is small enough to accommodate both murine tissues and meaningful regional variations, while remaining practical for specimen handling.

2.2 Design Approach. In Secs. 2.2.1–2.2.5, the design solutions that were implemented to satisfy the above mentioned requirements are presented.

2.2.1 Attachment System. Three attachment points per side were chosen to balance the size restriction of a 4 mm × 4 mm specimen with the increased size of the homogeneous deformation zone provided by four points per side. The attachment system was

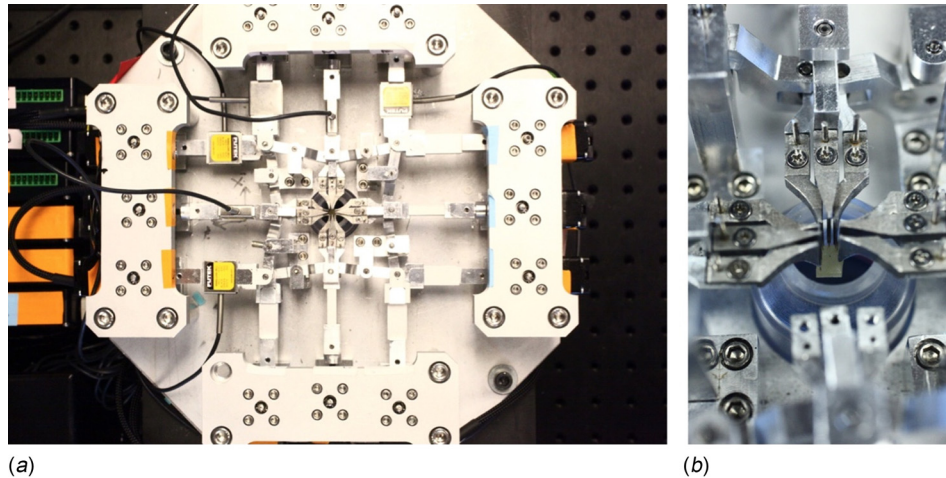


Fig. 2 (a) Top view of the device showing the specimen test area and (b) close up view of specimen mounted on actuation arms

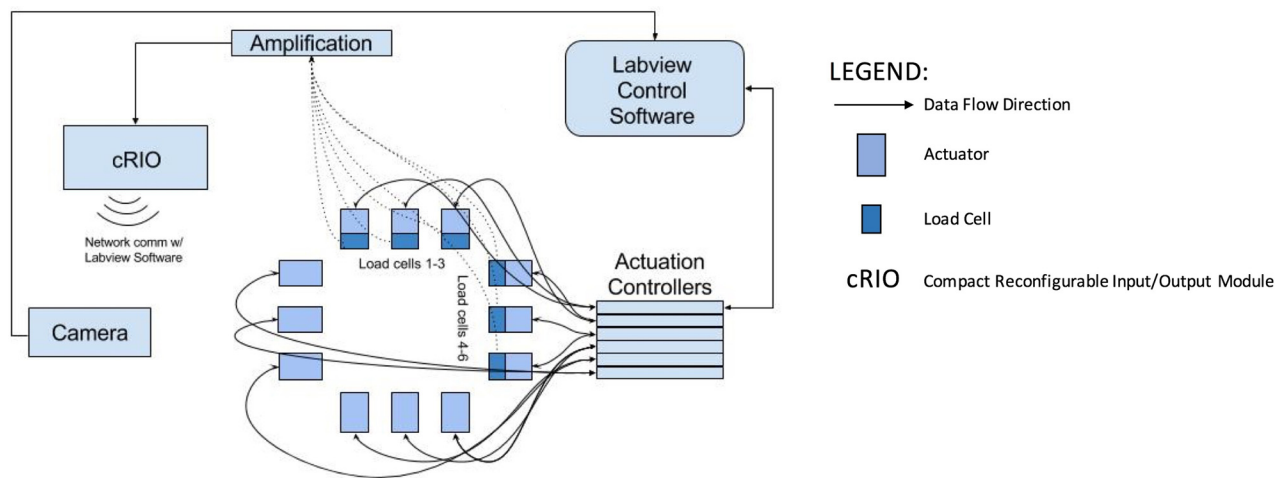


Fig. 3 Test system schematic showing the major hardware and software components of the device and the data interconnections between them

composed of three straight 200 μm diameter extruded stainless steel needles, attached to the specimen along each edge (Fig. 2).

2.2.2 Mounting Method. As mentioned above, the symmetry and spacing of the attachment points strongly influence the homogeneity of the deformation and stress within the specimen. In order to consistently achieve the required symmetric needle placement, the needles were attached with the assistance of a microscope equipped with a digital camera. The digital camera sent the live microscope view image to a computer monitor. A virtual template image of the correct, symmetric attachment pattern was superimposed on the microscope view image and aligned so it was centered on the specimen. This composite image was then used to guide the placement of the needle attachments. The target spacing between the attachment points on each side was 0.9 mm and the spacing between adjacent corner positions was approximately 0.78 mm. This spacing was enforced through the use of a custom assembly jig that guaranteed proper spacing of the attachment arms during specimen attachment and subsequent mounting onto the test system. Once mounted, specimens were submerged in a bath of phosphate-buffered saline (PBS) for preservation.

2.2.3 Actuation. The actuation system consisted of 12 actuators (Zaber model LAC10A-T4, Zaber Technologies, Inc.,

Vancouver, BC, Canada) placed three per side and able to fully act independently (Fig. 3). The actuators had an extension range of 10 mm, a location accuracy of 10 μm and maximum and minimum speed of 12 mm/s and 0.0145 $\mu\text{m/s}$, respectively. The actuators were attached to an array of Zaber A-MCB2 stepper motor controllers which connected directly into the computer unit hosting the main LabVIEW (National Instruments Corporation, Austin, TX) software suite. In order to achieve individual actuation at a small scale, bell-crank mechanisms on the outer actuation arms were used to translate displacement close to the center of the specimen. Refer to Appendix A for details on the design.

For measuring force response, six miniature S-beam load cells (Futek model LSB200—FSH00102, Futek Advanced Sensor Technology, Inc., Irvine, CA) were used on the first arm, between the actuator and the pivot point connecting the first and second arms (Fig. 3). The signals of the load cells were amplified via an op-amp and routed to an NI 9221 (National Instruments Corporation, Austin, TX) input module (Fig. 3). The input module transmitted the signals to the main LabVIEW VI through a local area network connection between the main host computer and a cRIO-9075 (National Instruments Corporation, Austin, TX) (Fig. 3). Four of the load cells were attached on four outer actuation arms (first, third, fourth, and sixth) between the first linkage of the bell crank and the actuator. Two of the load cells were

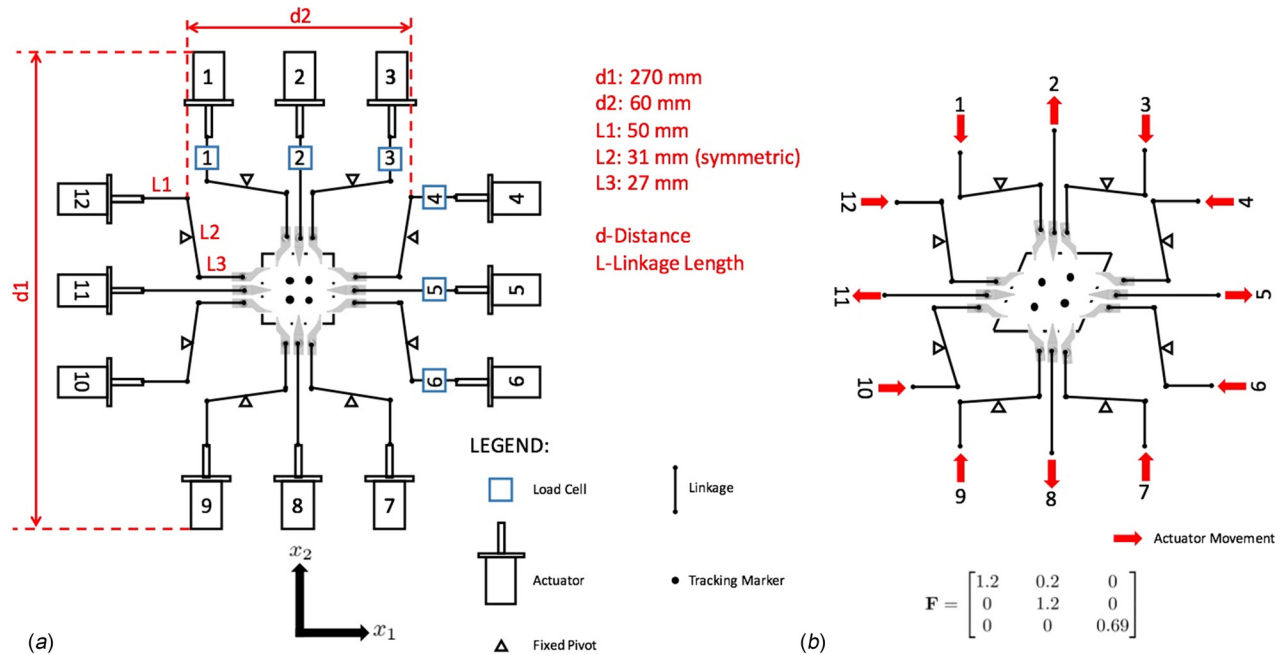


Fig. 4 (a) The components and major dimensions of the actuation system in the unloaded configuration. Also shown in (b) is how the system deforms under a generalized loading state.

attached to two of the middle actuation arms (second and fifth) between the actuators and an extension structure, which translated displacement from the actuators linearly to the specimen region (Fig. 4). The variance in placement of the load cells in the actuation line was necessary to optimize the performance of the actuation system. Furthermore, any effect on measurements due to positional differences was accounted for in the design and the ability to obtain accurate forces was not affected as the load cell measurements were used to analytically calculate the point force values at the specimen attachment points. Attached to the end of the bell-crank mechanisms (Appendix A) and extension arms were the tissue attachment links. The links were allowed to pivot freely so that the attachment points at the specimen may translate orthogonally to the actuation arm.

2.2.4 Image Feedback. To measure \mathbf{F} and provide feedback to the control system, a 2×2 array of markers were placed on the specimen surface inside of a $1 \text{ mm} \times 1 \text{ mm}$ region at the center of the specimen. A CCD camera with 1388×1038 pixel resolution (Guppy Pro F-146B, Allied Vision, Stadroda, Germany) was mounted under the main stage of the device (Fig. 3) and sent images of the marker region into the LabVIEW software at a rate of 100 Hz. The camera faced a mirror oriented at an angle of 45 deg to both the camera and the planar normal of the specimen. A fixed focal length lens in-line with a lens extender (Computar Model EX1.5C, Computar, Cary, NC) provided a net linear resolution of 459 pixels/mm. Since \mathbf{F} was controlled by feedback from the imaging system and the maximum marker positions were constrained by the size of the camera field of view, overall specimen strain was constrained by the pixel resolution and the camera field of view. For a $1 \text{ mm} \times 1 \text{ mm}$ square marker region, maximum extension was 200% in the horizontal direction and 125% in the vertical direction. Before the images from the camera were displayed in the LabVIEW window, they were processed to obtain maximum contrast between the markers and the specimen surface. This was done by setting the pixels correlating to the markers to the lowest intensity (0-bit) and setting those correlating to the tissue surface to the maximum intensity. With the mouse, the user then drew a rectangular pixel boundary in the specimen view window around each marker. The location of each marker was taken to be the centroid of the lowest intensity bits within the regions.

A center pixel was then calculated using the average horizontal and vertical pixel coordinates of the four marker positions. When the user entered the target \mathbf{F} , the associated target positions of the markers were calculated from this center pixel. From the initial and target positions, the target marker trajectory was obtained. Other systems have used digital image correlation (DIC) for deformation and strain measurements. Digital image correlation is a noninvasive imaging technique, which is capable of tracking the displacement of subtle surface features and can therefore be used to determine strain. However, the implementation of DIC for strain measurement in the present device would complicate marker tracking and add latency to the system to the detriment of deformation control accuracy.

2.2.5 Control System. As mentioned above, the control system needed to handle coupled, nonlinear responses despite large uncertainty in mechanical response parameters. Generally, the dynamics of a system can be expressed as

$$\dot{\mathbf{s}} = \mathbf{f}(\mathbf{s}, \mathbf{u}) \quad (3)$$

with $\dot{\mathbf{s}}$ being the time derivative of the system state vector \mathbf{s} , and \mathbf{f} being a function of state vector and controller input vector \mathbf{u} . For a control system that is linear with respect to its inputs, the matrix form of this equation is

$$\dot{\mathbf{s}} = \mathbf{A}\mathbf{s} + \mathbf{b}\mathbf{u} \quad (4)$$

Sliding mode controllers (SMC) are a type of control system where the input vector is a discontinuous function of the system state vector [17]. In these controllers, provided certain requirements on the size of the input and state vectors are met, there exists a reachable manifold in the state space, denoted by $\sigma = 0$, σ being defined as

$$\sigma = \sum_{i=1}^n c_i s_i, \quad c_i \text{ const}, \quad c_n = 1 \quad (5)$$

on which the dynamics of the system only depend on the constants, c_i and not on the mechanical parameters, a_{ij} . On this surface, the dynamics equation can be reformed as

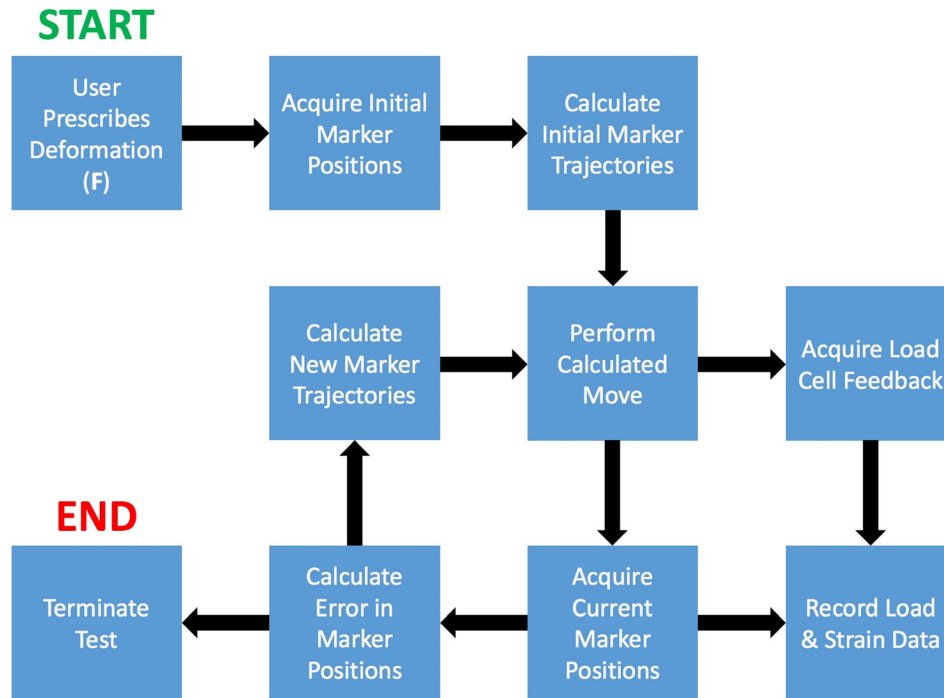


Fig. 5 A schematic of control algorithm process flow during run-time

$$\begin{aligned} \dot{s}_i &= s_{i+1} \quad i = 1, \dots, n-2 \\ \dot{s}_{n-1} &= -\sum_{i=1}^{n-1} c_i s_i \end{aligned} \quad (6)$$

in which dependence on mechanical parameters (a_{ij}) disappears [17]. This is an attractive property for a control system and fits the design objective perfectly. This surface is called the sliding surface and the system, once on the surface, is said to be in sliding mode. Once the system is in sliding mode, it can drive the state vector toward any desired value prescribed by the user. Designing the SMC involves designing the sliding surface such that the dynamics of the system on the surface are acceptable, and then designing the switching logic so the discontinuous control modes drive the state trajectories of the system to the sliding surface [18]. Further detail on the mathematical background of SMC and on their design can be found in Appendix B.

In the case of the present device, SMC controlled the individual linear actuators to bring the tissue to the desired deformation. The marker positions were used to determine the state of the system as they provided full state feedback, greatly simplifying the SMC design. The major steps of the control system are as follows (Fig. 5): First, the user inputs the desired \mathbf{F} ; then the system determines the initial locations of the markers and calculates the initial marker trajectories. The control system then enters a loop in which it performs the calculated marker move, acquires feedback on load cell and marker information, records this feedback as load and strain data for later analysis, and then calculates new marker trajectories based on the difference in current versus prescribed marker positions. This loop is repeated until the error in current versus prescribed marker positions goes to zero indicating the desired deformation has been applied, at which point the test is terminated.

The control algorithm was developed in the MATLAB programming environment (MathWorks, Natick, MA) in parallel to the development of the hardware system. The isolated development of the control software allowed for the theoretical aspects of the controller to be verified in an environment free of error from subtle inaccuracies and imperfections, which naturally exist within realistic systems.

In order to estimate the response of tissue material in the simulated environment, specimens were modeled as systems of highly damping, interconnected springs between nodes. The points of attachment between the system and the specimen as well as the pivot points at the end of the actuation arms were also included in the simulated environment (Fig. 6). Varying parameters, such as the damping of individual springs, allowed for testing the controller against various levels of material stiffness and isotropy. Optimum control parameters were selected by visualizing the tracking error surface over a range of simulated material parameters and controller parameters. The chosen control parameter set were those that minimized the tracking error.

The optimum controller parameters determined in the above mentioned process were able to accommodate a wide variety of tissue types and were set as defaults in the LabVIEW VI. However, as it was impossible to predict how the device may be used in the future, the user was given access to the controller parameters in the event tuning became necessary. The tuning process follows that outlined above and involves visualizing and subsequently minimizing the tracking error by varying the parameter set. The order and amount by which parameters should be varied are according to standard controller tuning methods. Refer to Appendix C for further details.

Beyond providing an environment for controller parameter tuning, the simulated test environment provided an opportunity to devise a strategy for mitigating the over-actuated nature of the control problem, i.e., that the size of the input vector \mathbf{u} is larger than the size of the tracked state vector \mathbf{s} (12 actuators controlling the position and velocity of four markers). This problem was overcome by decomposing the position error of each marker into x_1 and x_2 components. This allowed the controller to send each actuator an input u_i corresponding to the measured error in a unique tracked state variable s_i , which eliminates the over-actuated problem. Beyond removing the over-actuated issue, decomposing the error into x_1 and x_2 components also allowed the control system to be agnostic to the type of deformation prescribed. Because each independent linear actuator was solely responsible for eliminating the error in a unique component of the system state error vector, the motion of each actuator was only a function of the state error vector component it was uniquely responsible for and had no

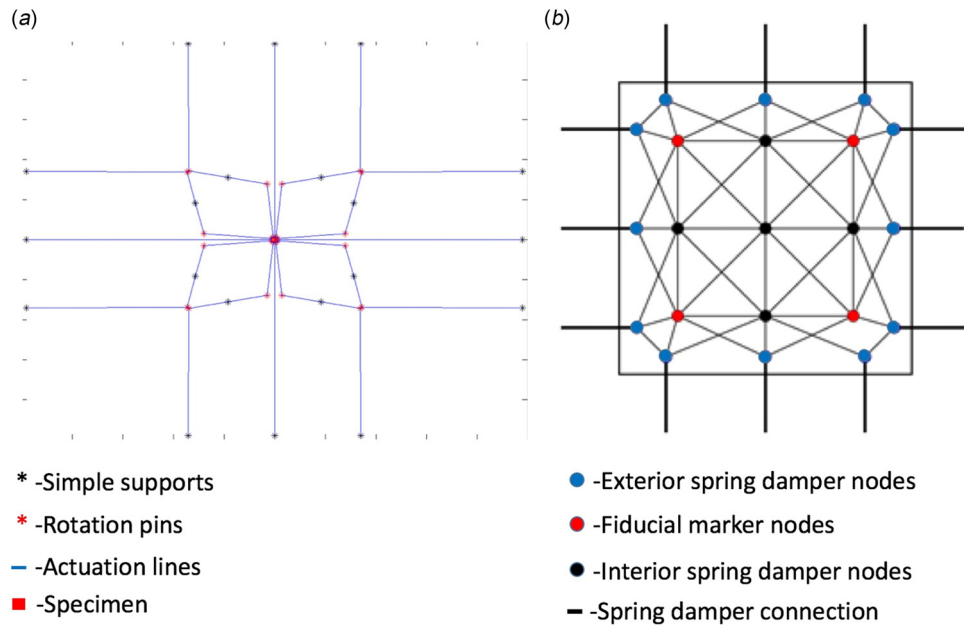


Fig. 6 Details of the system components included in the simulation of the device performance: (a) actuation system components and (b) specimen spring damper model

dependence on the type of deformation requested. Corner actuators along the x_1 axis (Fig. 4, actuators 4, 6, 10, 12) were responsible for eliminating their corresponding marker x_1 position error, while corner actuators along x_2 (Fig. 4, actuators 1, 3, 7, 9) eliminated x_2 position error. Center actuators (Fig. 4, actuators 2, 5, 8, 11) eliminated the averaged velocity error between their corresponding markers. This novel approach was fundamental in designing a control system robust and flexible enough to enforce arbitrarily prescribed deformation.

2.3 Design Evaluation. The evaluation of the design was two-fold. First, the control system's ability to enforce the user requested deformation gradient and to do so homogeneously was analyzed. Then, the device was used to perform test cases on various types of materials for validation and performance benchmarking.

2.3.1 Finite Element Simulations. In order to determine the level of stress field homogeneity within the marker region for a nonlinear, anisotropic specimen, finite element (FE) simulations of the device under different loading conditions were performed. These simulations were based on and utilized the same methods as in Refs. [3] and [19], with modifications made to account for the current specimen geometry. Briefly, simulations were performed in ABAQUS (Simulia, RI) on a $3.5 \text{ mm} \times 3.5 \text{ mm}$ specimen, using a structurally based constitutive model with material parameters taken from Ref. [19] for bovine pericardium. Three point load attachments per side were used, with the loads applied by displacing the point attachments to precisely reproduce the general planar biaxial deformation state.

2.3.2 Control System Performance Analysis. As stated above, target and actual marker position histories were recorded in real time. Time-averaged mean and standard deviation of the tracking error between target and actual marker position were then computed. The deformation gradient tensor was calculated using standard bilinear FE methods [10] for the target and actual marker positions at each recorded frame. \mathbf{F} was determined at any point within the element formed by the four fiducial markers. Homogeneous deformation of the specimen was defined as a deformation field where the components of \mathbf{F} at any given point in the measurement region were within a certain tolerance value of the components of \mathbf{F} at any other point in the region. To assess

deformation homogeneity, \mathbf{F} was computed for each marker at the end deformation state of a test. Then, each component of \mathbf{F} was interpolated through the measurement region with the above mentioned interpolation method, using the markers as the interpolation nodes. This produced maps of the components of \mathbf{F} at each point in the measurement region, which were then plotted using a density plotting method to evaluate homogeneity.

As an additional investigation of the homogeneity performance of the device, a 3×3 array of markers bounding an approximately $1.5 \text{ mm} \times 1.5 \text{ mm}$ region was applied to a bovine pericardium specimen. The specimen was mounted onto the device and protocols involving each type of biaxial deformation were applied with the control system using the four corner marks for control purposes while the image feedback system recorded the position of all nine markers during the test. The position of the nine markers was then used to perform a biquadratic interpolation of the components of \mathbf{F} through the measurement region. Statistical measures of these full field values were computed to assess homogeneity. Finally, the experimentally prescribed \mathbf{F} was applied to the positions of the nine markers in the reference state, and the resulting positions were plotted alongside those of the markers in the deformed state at the end of the protocol.

2.3.3 Device Validation. In order to confirm that the device functioned as designed, an isotropic polymer with a nonlinear response was used to perform validation tests against another biaxial system [4]. Liquid polyurethane rubber of hardness 20A was acquired from SmoothOn Inc., (Macungie, PA). The polyurethane was mixed and cured in lab to form solid sheets. From one of the sheets, a square region was stamped out with a razor. The square sample was measured at $4.53 \times 4.51 \times 1.179 \text{ mm}$. From the same sheet, another square region was cut out and tested on another biaxial testing device [4] for validation.

2.3.4 Exemplar Soft Membrane Tissues Evaluated. Performance benchmark tests were conducted on three types of biological tissues. Four regions of the ovine aortic leaflet (one nodular region, two belly regions, and one basal attachment region) were selected for the first tissue type. These regions were chosen because their mechanical response varies widely [14] and they thus served as an established test bed for evaluating the ability of the device to determine regional variation in tissue properties. The second tissue type was bovine pericardium, which was selected to

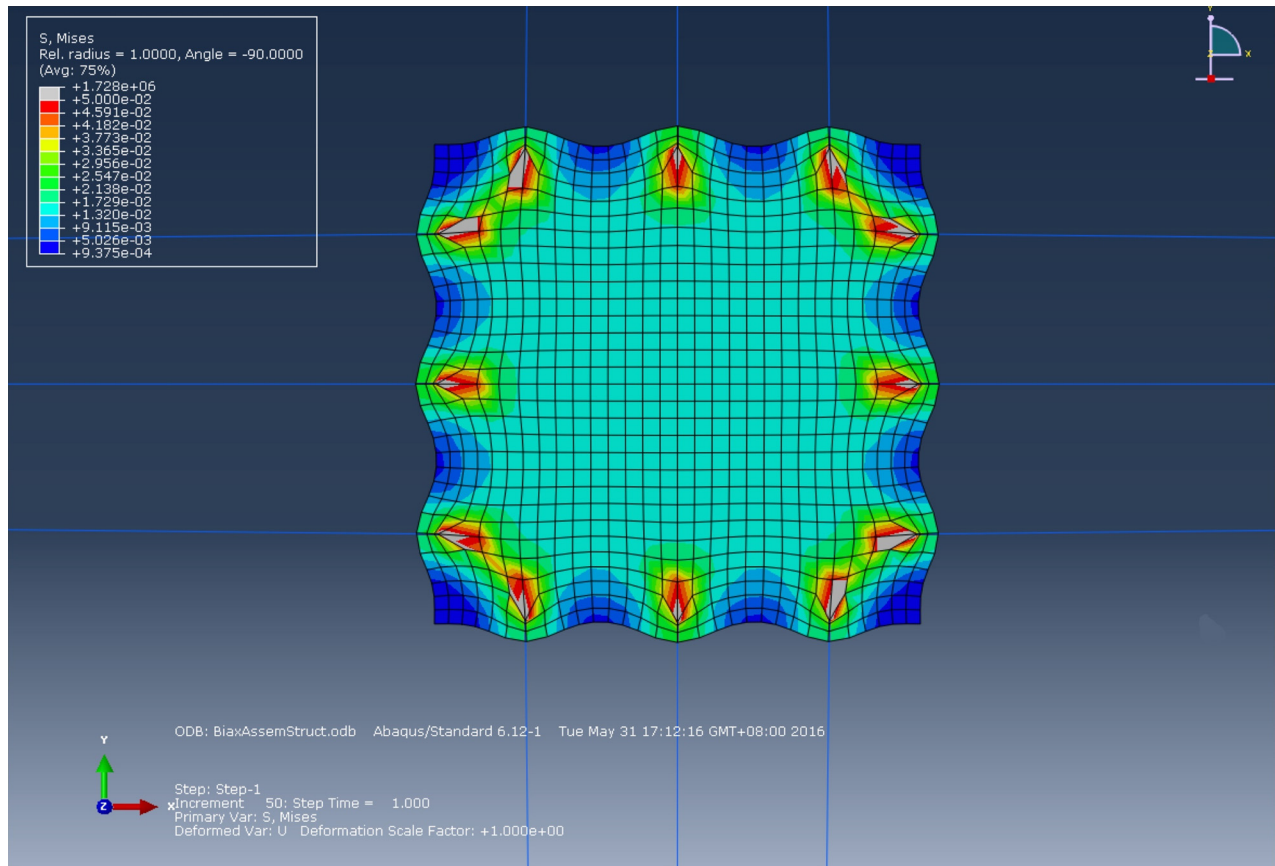


Fig. 7 FE simulation results for the Von Mises stress index over the entire specimen, with the each pin displaced 0.5 mm either along the x_1 or the x_2 , depending on its side. Results clearly show a high degree of stress field homogeneity, with the stress concentrations induced by the pin attachments producing only local effects.

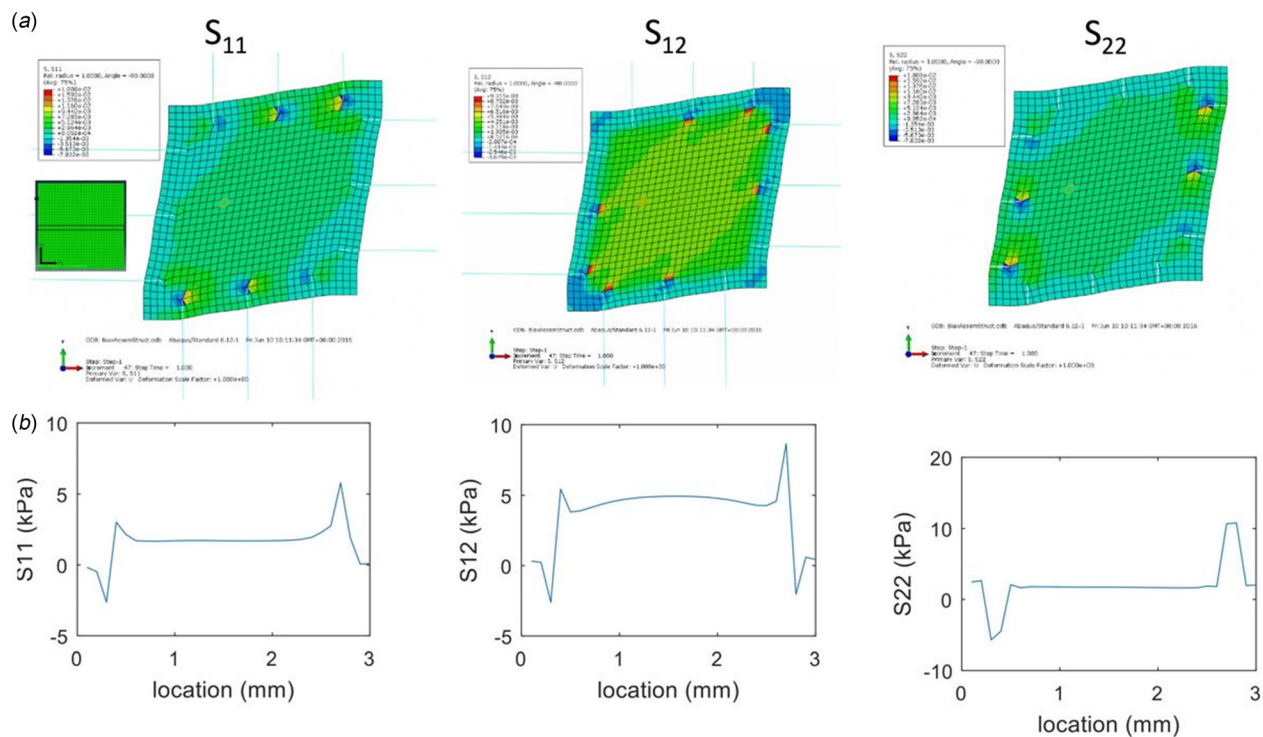


Fig. 8 (a) FE results for simple shear for each component of S and (b) resulting plots of the components of S versus x_1 , using the elements shown in the inset in (a)

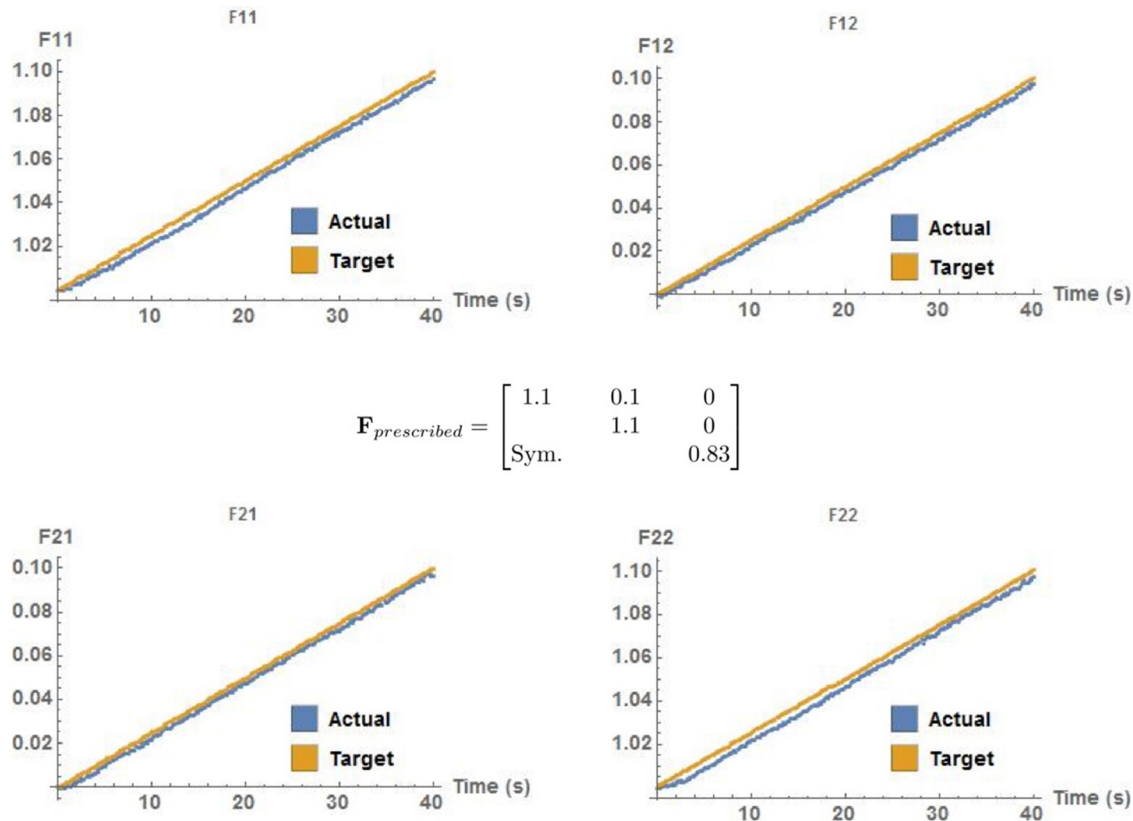


Fig. 9 Plots of actual versus prescribed deformation gradient component for a general planar biaxial deformation

validate the device with a tissue commonly used in clinical practice, e.g., bioprosthetic heart valves. Finally, murine aorta was used for the third tissue type to examine the capability of the device to test small specimens with arbitrary, user-prescribed deformation gradients.

2.3.4.1 Aortic valve leaflet. Frozen adult ovine hearts were obtained from Animal Technologies (Tyler, TX). The hearts were thawed in 4°C over approximately 36 h. After thawing, the non-coronary leaflet was removed from each. Four regions approximately 4 mm × 4 mm in size were stamped out with a straight edge razor blade. These four regions were numbered 1, 2, 3, and 4 and correspond to the nodulus region, the basal attachment region, and the two peripheral regions with region 3 corresponding to the left peripheral region and region 4 corresponding to the right peripheral region. Regions were stored in −80°C until tested. The specimen's circumferential and radial dimensions (L1, L2) were measured with digital calipers under a microscope. Thickness (L3) measurements were made using a micrometer under no optical assistance. The specimens were marked by carefully adhering particles of polyethylene terephthalate powder (glitter) of approximately 40 μm in diameter into a square formation bounding approximately a 1 mm × 1 mm region as described above.

Specimens were mounted on the device so that the preferred fiber direction was aligned along one of the test axis. Small normal strain values ($\lambda_1, \lambda_2 > 1$) were used to determine a preliminary tissue response. The values of λ_1 and λ_2 were incrementally increased until a membrane tension of 90 N/m along one of the axes was achieved. The specimen then underwent ten preconditioning cycles at this reference deformation. The strain was then incrementally increased along the more compliant of the two axes to achieve an equi-biaxial membrane tension of 90 N/m. This value of \mathbf{F} was used to for an additional ten preconditioning cycles. After these preconditioning cycles, a single cycle to the final value of \mathbf{F} was performed for data collection.

2.3.4.2 Pericardium. Fresh bovine pericardium was acquired from hearts excised at Harvest House Farms, Johnson City, TX. The tissue was brought to the lab no more than 1 h after excision. A 6 mm × 6 mm region was isolated, submerged in PBS, and stored at 2°C. Five days later, from this region, a specimen was stamped out measuring 4.78 mm × 4.52 mm × 0.851 mm along the x_1 , x_2 , and x_3 axes, respectively. As a convention, the x_1 axis was designated to be along the direction with which the visible fiber orientation predominantly aligned. The x_2 -axis was designated to be perpendicular to x_1 and along the plane described by the largest surface area of the specimen.

2.3.4.3 Murine aorta. Murine specimens were obtained from the Animal Resources Center at UT Austin after the specimens had been perfused with paraformaldehyde. The aorta was excised and submerged in PBS and stored at 2°C. No more than 24 h passed before a small square specimen from the anterior region of the ascending aorta was stamped out with a razor blade. The circumferential, radial, and longitudinal dimensions were measured to be 4.32 mm × 4.24 mm × 0.263 mm, respectively. The circumferential direction was aligned with the x_1 test axis and the radial direction aligned with the x_2 -axis. Once the specimen was mounted onto the device, a load control procedure similar to the one outlined above for the aortic valve leaflet was used to determine deformation gradients, which would produce a 60–90 N/m tension response

Table 1 Deformation modes and max strain levels used in tracking error performance analysis

	General	Simple extension	Simple shear
\mathbf{F}	$\begin{bmatrix} 1.1 & 0.1 & 0 \\ & 1.1 & 0 \\ \text{Sym.} & & 0.83 \end{bmatrix}$	$\begin{bmatrix} 1.2 & 0 & 0 \\ & 1.2 & 0 \\ \text{Sym.} & & 0.69 \end{bmatrix}$	$\begin{bmatrix} 1 & 0.5 & 0 \\ & 1 & 0 \\ \text{Sym.} & & 1 \end{bmatrix}$

Table 2 Tracking error mean for the deformation modes shown in Table 1 (unitless)

Component	General	Simple extension	Simple shear
F11 mean	-3.22×10^{-3}	-2.12×10^{-3}	-6.30×10^{-4}
F11 STDEV	8.06×10^{-4}	1.73×10^{-3}	3.56×10^{-3}
F12 mean	-2.63×10^{-3}	-3.38×10^{-3}	-8.99×10^{-3}
F12 STDEV	5.94×10^{-4}	4.17×10^{-3}	3.35×10^{-3}
F21 mean	-2.30×10^{-3}	9.27×10^{-4}	-3.53×10^{-3}
F21 STDEV	6.24×10^{-4}	1.28×10^{-3}	4.81×10^{-3}
F22 mean	-3.57×10^{-3}	-3.00×10^{-3}	-1.28×10^{-3}
F22 STDEV	8.72×10^{-4}	1.04×10^{-3}	5.39×10^{-3}

in shear. The \mathbf{F} values from the load tests were then used as initial deformation gradients for subsequent strain control tests.

3 Results

3.1 Finite Element Simulations. Results from the finite element simulations indicated that the device produced a reasonably

homogeneous stress field under equi-biaxial strain (Fig. 7). Stress homogeneity under simple shear was also investigated by plotting the components of \mathbf{S} versus x_1 coordinate over elements located in the center of the specimen (Fig. 8). These results show that the value of each component of \mathbf{S} is relatively constant within the inner $1 \text{ mm} \times 1 \text{ mm}$ marker range, with this being especially true for the normal stress components.

3.2 Control System Performance. The control system of the device was able to control the in-plane deformation gradient tensor in real time. Even in the challenging case of general planar biaxial deformation (Fig. 9), the controller response exhibited minimal error and oscillation. During tests of polyurethane specimens, tracking error statistics for this and several other common deformation modes (Table 1) were collected (Table 2) and demonstrate the accuracy of the real time control system. Moreover, in light of a system imaging resolution of 0.00218 mm/pixel , the computed error statistics illustrate the ability of the controller to achieve errors on the order of pixel size, i.e., it prescribes the required deformation as accurately as the system imaging resolution allows.

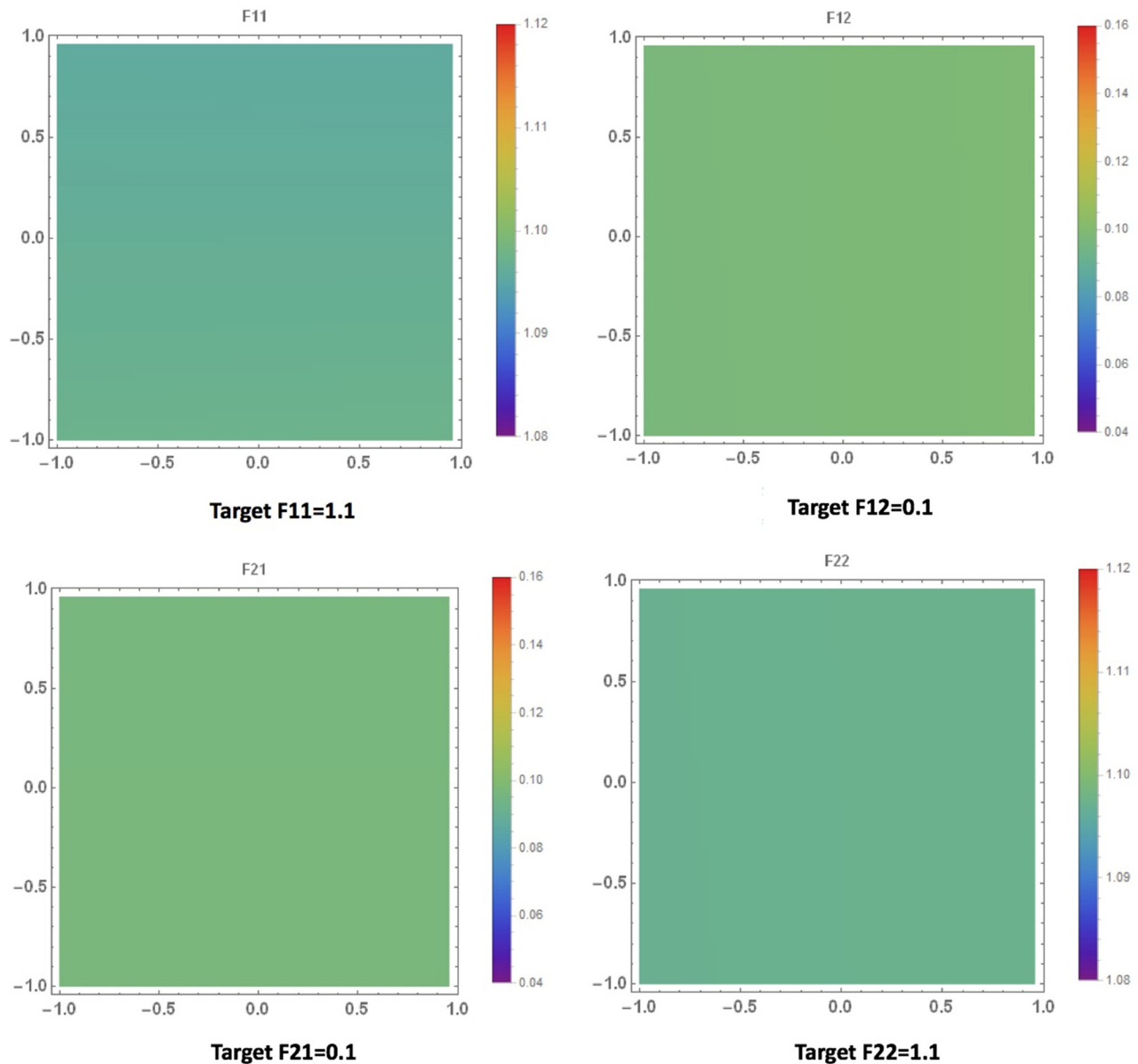


Fig. 10 Plots of deformation gradient tensor components at maximum deformation interpolated throughout the measurement region for a general planar biaxial deformation, showing good uniformity in responses

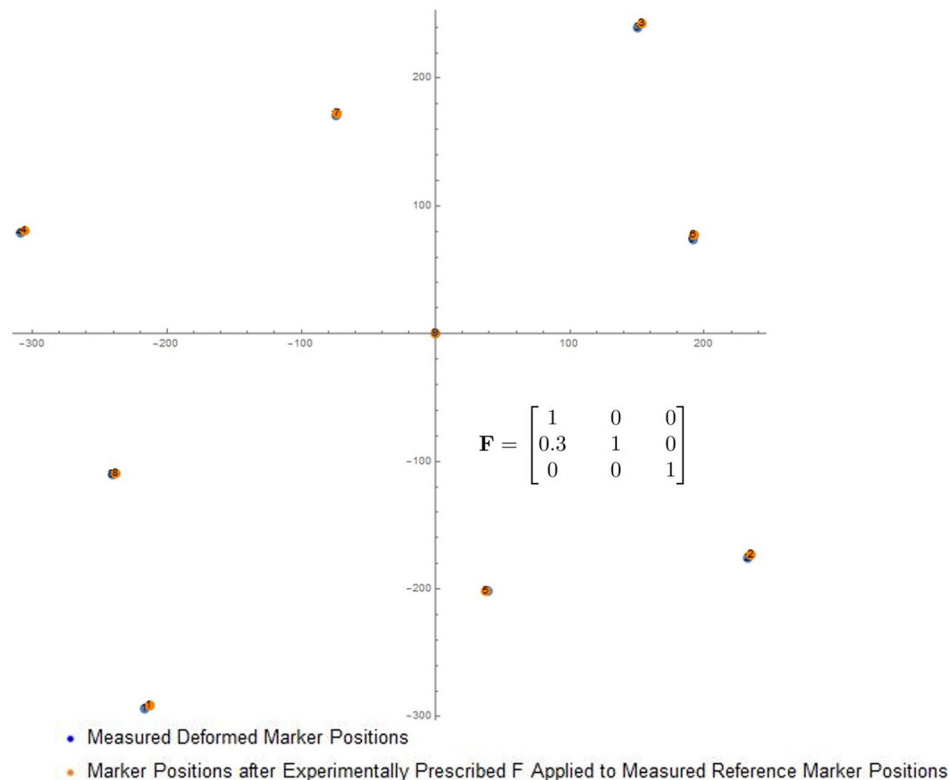


Fig. 11 The measured positions of the 3×3 marker array in the deformed state versus after a representative experimental \mathbf{F} was applied to each measured position of the array in reference state for a bovine pericardium specimen. The close agreement in final positions indicates that the strain field as controlled by the 2×2 array was relatively homogeneous over the entire region.

In addition to the controller's good tracking performance, it also displayed good deformation gradient homogeneity results from polyurethane specimen tests. The results from the bilinear interpolation of the deformation gradient indicate that, even when applying a general planar biaxial deformation, the resulting deformation field had a high degree of homogeneity (Fig. 10). It is worth noting here that the term "bilinear" is somewhat of a misnomer. The interpolation method is linear in the x_1 and x_2 directions meaning the total deformation can vary quadratically and the strain linearly within the element. Quantitative measures of full field mean and standard deviation values of the deformation gradient further underscore the homogeneity of the applied deformation.

In addition to the bilinear studies, the biquadratic interpolation of the 3×3 marker array placed on a bovine pericardium specimen also shows the ability of the device to apply \mathbf{F} homogeneously even when the material under test is anisotropic and not exactly homogeneous. Though the system only uses four markers in the control algorithm, it places all nine markers in the position required by the prescribed \mathbf{F} accurately (Fig. 11), with average marker position errors of 0.0063 ± 0.0011 mm. Statistics computed on the biquadratically interpolated \mathbf{F} field provide quantitative support for the conclusion that the device applies \mathbf{F} accurately and homogeneously. Thus, these results underline the ability of the device to accurately and homogeneously apply a general, in-plane deformation by adjusting to the response of the tissue in real time.

3.3 Device Validation. The validation study on the polyurethane yielded good qualitative agreement between the established system and the new device. Because separate specimens were used on the two devices, data for detailed quantitative

comparison of a single specimen tested on both devices were not available. Nonetheless, the quantitative agreement of the stress-strain response is verification that the new device performs as designed.

3.4 Soft Tissue Test Cases

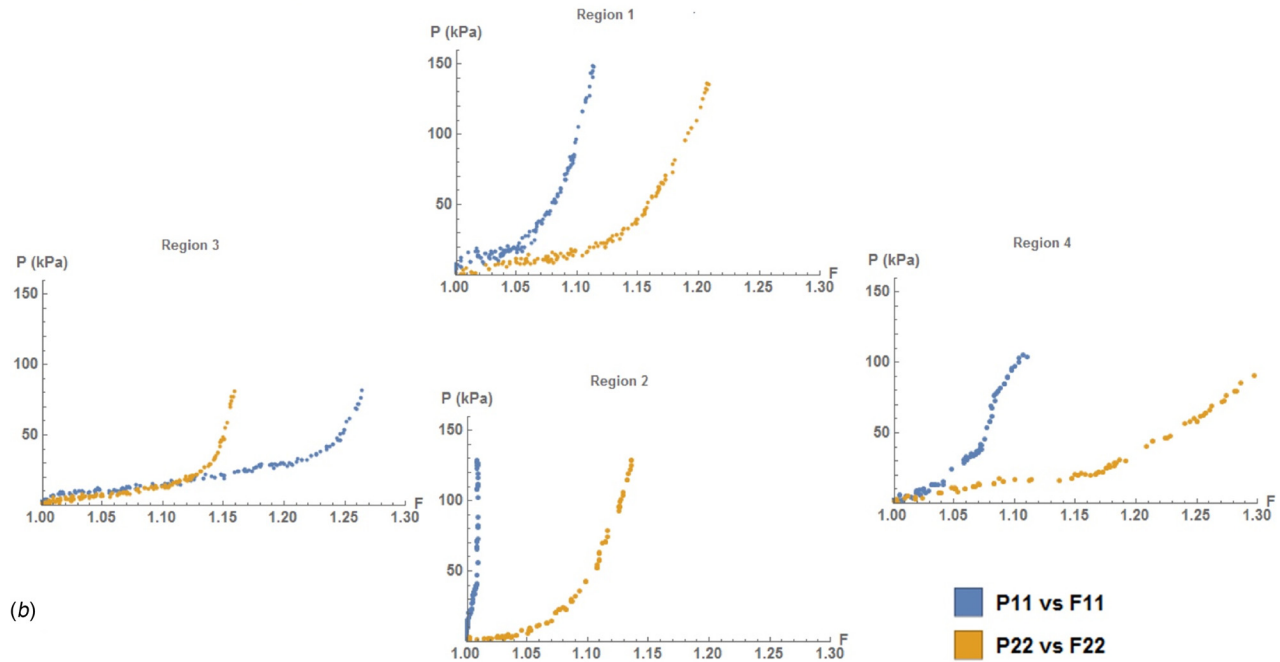
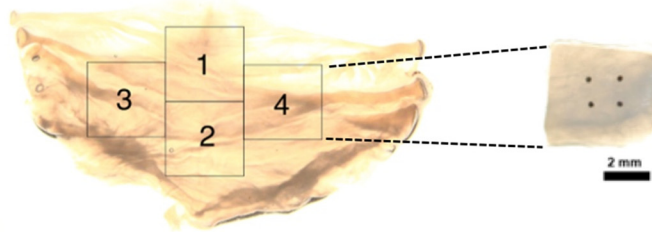
3.4.1 Aortic Valve Leaflet. Consistent with previous results [14], the aortic valve leaflet exhibited an anisotropic, nonlinear mechanical response that varied within the leaflet. Specifically, the basilar region was much stiffer in both the radial and circumferential directions than the nodular region (Fig. 12). Beyond being consistent with past findings, these results demonstrate how the small specimen size range of the device enables successful investigation of the regional variation in mechanical response of the aortic valve leaflet.

In addition to the device investigating the regional response of the aortic valve leaflet to simple extension deformation, the device was also able to apply a prescribed simple shear deformation and record the response (Fig. 13). This further confirms the device's capability to fully explore the mechanical response space and precisely replicate any desired loading state.

3.4.2 Bovine Pericardium. In line with past studies [20], the bovine pericardial tissue was also nonlinear and anisotropic in its mechanical response (Fig. 14). However, as expected, it was not as anisotropic as the aortic valve leaflet due to more a randomly distributed collagen fiber architecture.

3.4.3 Murine Aorta. Due to the challenges of its small size, the murine aorta has typically been tested using pressure inflation methods combined with uniaxial extension [21,22] where there is

(a)



(b)

Fig. 12 (a) Location of specimen subregions in aortic valve leaflet, showing an example of marked subregion of specimen and (b) resulting mechanical responses of the subregions

no control of the in-plane shear. In contrast, the present device was able to apply a prescribed in-plane shear to the murine aorta and measure the resulting stress response (Fig. 15). This result represents an important step toward a more robust biomechanical evaluation of the genetically and biochemically manipulable murine model.

4 Discussion

4.1 Overview. We have developed a novel planar biaxial testing device capable of independent control of all the components of \mathbf{F}_{2D} in a homogeneously deformed $\sim 1 \text{ mm} \times 1 \text{ mm}$

central region of a $\sim 4 \text{ mm} \times 4 \text{ mm}$ specimen. Devices with image based real-time control of the extensional components of \mathbf{F}_{2D} have existed for years [20] but remain limited in their ability to produce in-plane shear, relying on experimental setup and test material structure [5] to produce uncontrollable and unpredictable in-plane shear strains. The new device overcomes these difficulties by controlling each individual specimen attachment point and using real-time image feedback coupled with a robust control scheme to account for unpredictable mechanical response. This approach allows the device to enforce any arbitrary, prescribed \mathbf{F}_{2D} needed for constitutive modeling. These capabilities enable

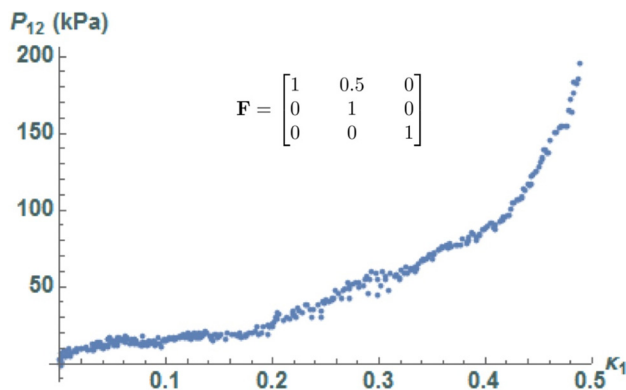


Fig. 13 Response of the basilar region of the aortic valve leaflet to a simple shear deformation

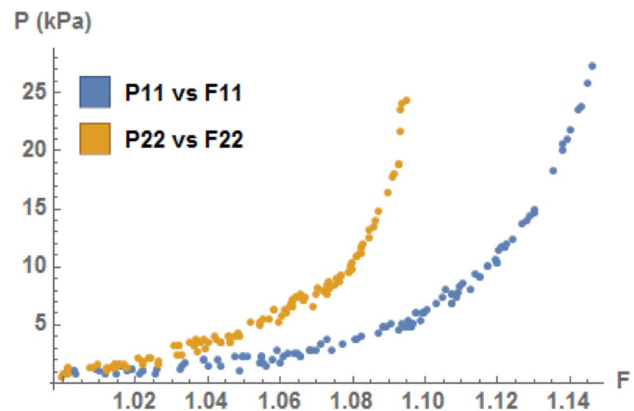


Fig. 14 Mechanical response of pericardial specimen to extension deformation

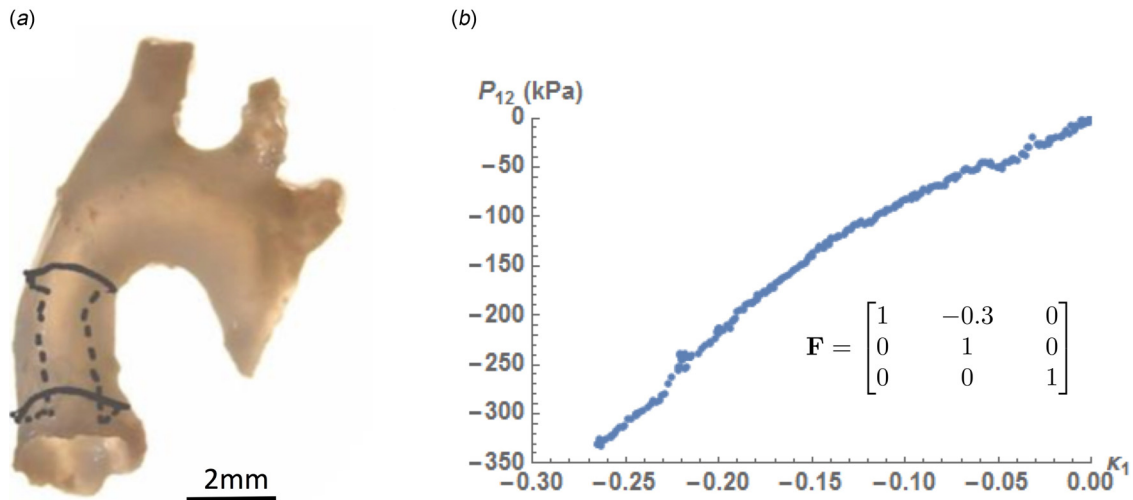


Fig. 15 (a) Location of specimen in murine aorta and (b) shear stress versus shear deformation response

the device to serve as a platform for developing and validating inverse models of larger biological structures as well as exploiting data from murine models of vascular tissues. The device displayed excellent accuracy (Fig. 9 and Table 2) and deformation field homogeneity (Figs. 10 and 11) with an average error in \mathbf{F}_{2D} component of 2.93×10^{-3} and an average component full field standard deviation of 2.96×10^{-4} . Moreover, example tissue types illustrated that the device was able to test specimens as small as 3 mm per side (Figs. 12(b) and 15).

These capabilities are becoming increasingly relevant as inverse models of tissue biomechanics grow in popularity as a means for constructing simulations of tissue behavior for medical, surgical, and pathophysiological applications. This is especially true as inverse models are used more and more for in vivo assessment purposes with the ultimate goal of clinical applications [8,23,24]. Clearly, the results of these in vivo inverse models must be thoroughly validated before becoming part of mainstream clinical practice. While verification of the results and material constants obtained with inverse models is obviously important, Zhang et al. underscore the necessity of first determining the functional form of Ψ before proceeding to simulation [3]. Inverse models are powerful tools for determining in vivo material parameters for a given Ψ form, but they are poorly suited for defining functional forms. In contrast, in vitro approaches are well established techniques for establishing the form of Ψ [14,25–27]. Thus, the device can generate in vitro data for the development of the functional form of Ψ , the parameters of which can be found with inverse models and verified with further data from in vitro testing with the device. For example, in a recent study, we showed how in vitro mechanical data can be used to directly validate in vivo material behaviors derived from fiducial markers in the mitral heart valve leaflet [28].

Beyond verifying inverse models, the ability to test murine tissues with controlled, prescribed loading paths (including in-plane shear) is an improvement over the traditional techniques of extension and pressure inflation [21,22] and represents an exciting opportunity to conduct robust investigation into the influence of biochemical and genetic factors on the biomechanics of vascular tissues. A particular area of interest is in the development and treatment of atherosclerosis, for which the murine model has been used extensively, but biomechanical evaluations have been limited by the difficulty of testing the small vascular tissues [29,30]. While biaxial evaluations are preferable, extension/pressure inflation is still needed for evaluating the aortic arch due to the difficulties induced by the curved geometry and the high loads needed to replicate in vivo conditions.

4.2 Limitations. While the results presented for this device clearly demonstrate its ability to meet its stated design objectives, a potential further study of its performance would be using DIC to perform a high resolution investigation of the homogeneity of the deformation field in the measurement region. While this granular information would be informative, it is worth reiterating that the results from bilinear and biquadratic interpolations strongly support the conclusion that the device applies deformation with a good degree of homogeneity. Furthermore, while the device can tolerate some reasonable variations in material behaviors in the measurement region, large variations will result in heterogeneities in the deformation field that are beyond the ability of this or any device to control. Thus, care should be used in the tissue location and selection procedures. Finally, precise placement of specimen attachment pins is critical for achieving good homogeneity results. While the use of a spacing jig aids in accurate spacing and placement of the pins, its use adds to the time required to conduct an experiment.

4.3 Conclusions. In summary, we have designed, constructed, and validated a novel planar biaxial testing device. This device actuates each individual specimen attachment point and overcomes uncertainties in the specimen mechanical response with a robust, real-time controller, allowing it to enforce any prescribed \mathbf{F}_{2D} . These features result in a device capable of testing specimens as small as 3 mm \times 3 mm and applying up to 200% extensional strain or up to ± 25 deg shear angle with errors in prescribed \mathbf{F}_{2D} as low as 2.93×10^{-3} and standard deviation of the full field value of prescribed \mathbf{F}_{2D} of 2.96×10^{-4} . These specifications further underscore the exciting potential of this new device to construct and verify constitutive models of soft, biological tissues, with particular emphasis on inverse model validation and murine tissue testing.

Funding Data

- National Heart, Lung, and Blood Institute (Grant No. R01HL119297).

Appendix A: Bell-Crank Mechanism

Bell-crank mechanisms are used to change the line of action of an applied force. The mechanisms used in the device (Fig. 16) reverse the direction of force application with a one-to-one relationship between input and output displacement. This one-to-one

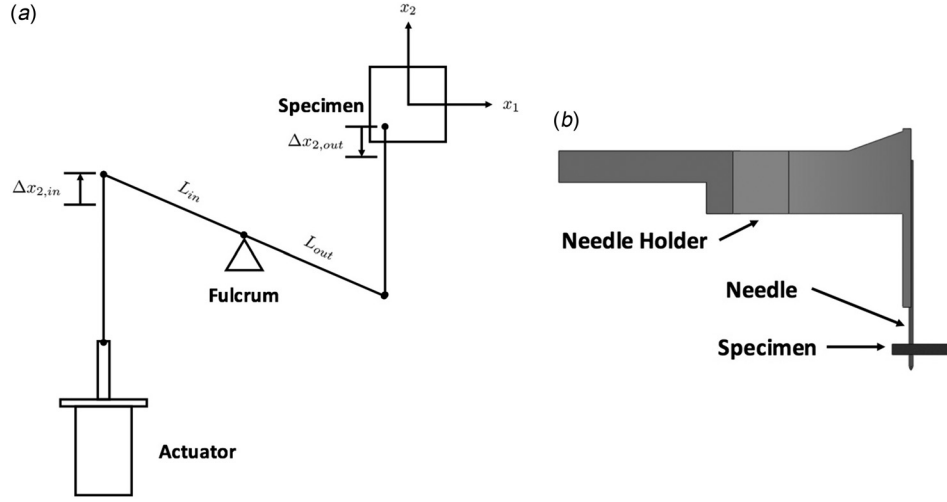


Fig. 16 (a) A schematic of the bell-crank mechanism used in the device outlining geometric relationships used to design a one to one relationship between input and output displacement and (b) close up of the needle holder, showing the needle and specimen

ratio between $\Delta x_{2,in}$ and $\Delta x_{2,out}$ is enforced by design through equating input and output lengths of the crank ($L_{in} = L_{out}$). Bell-crank mechanisms were used in the design of the device to circumvent the difficulty of individually actuating three attachment points per specimen side spaced less than a millimeter apart. Clearly, such a small spacing between attachment points eliminates the possibility of a simple actuator layout. The bell-crank mechanisms solve this problem by allowing the designer to select the distance between the actuator line of action and the attachment arm line of action needed for a straightforward actuator layout.

Appendix B: Theory and Design of Sliding Mode Controllers

B.1 Statement of Control Problem

The objective of the control system is to drive the state vector \mathbf{s} to some user prescribed value \mathbf{s}_d by driving the error $\tilde{\mathbf{s}} = \mathbf{s} - \mathbf{s}_d$ to zero given initial conditions $\mathbf{s}_d(0) = \mathbf{s}(0)$. Expressing the scalar equation of state vector σ (Eq. (5)) in terms of the state error vector yields the simple equation

$$\sigma = \left(\frac{d}{dt} + \gamma \right)^{n-1} \tilde{\mathbf{s}} \quad (B1)$$

where γ is a strictly positive constant and n is the relative degree between the input \mathbf{u} and \mathbf{s}_d . Thus, driving the error vector to zero given the above initial conditions is equivalent to controlling the state vector such that the associated scalar equation always remains along the manifold $\sigma = 0$. This simplification trades an n th order vector system for a first-order scalar problem [31]. Again, this manifold, $\sigma = 0$ is called the sliding surface and is an invariant set given the initial conditions $\mathbf{s}_d(0) = \mathbf{s}(0)$. The control law required to stay on the sliding surface is that for $\sigma \neq 0$

$$\frac{1}{2} \frac{d}{dt} \sigma^2 \leq -\eta |\sigma| \quad (B2)$$

where η is a strictly positive constant. This discontinuous control law guarantees all state vector trajectories point toward the sliding surface and that the distance to the surface is constantly decreasing [31].

B.1.1 Control Effort on the Sliding Surface-Equivalent Dynamics. As stated above, the first step in designing the SMC is constructing the control effort on the sliding surface such that

the system dynamics are acceptable. This can be accomplished through the use of equivalent dynamics. In sliding mode, the dynamics of the system are

$$\dot{\sigma} = 0 \quad (B3)$$

The equivalent control effort is found by solving the above equation under the formal assumptions that the control law is continuous and the mechanical response parameters are perfectly known [31]. For the illustrative example of $n = 2$ and $\tilde{\mathbf{s}} = \mathbf{f} + \mathbf{u}$

$$\dot{\sigma} = \ddot{\mathbf{s}} - \ddot{\mathbf{s}}_d + \gamma \dot{\tilde{\mathbf{s}}} \quad (B4)$$

which simplifies to

$$\dot{\sigma} = \mathbf{f} + \mathbf{u} - \ddot{\mathbf{s}}_d + \gamma \dot{\tilde{\mathbf{s}}} \quad (B5)$$

Thus, the equivalent control, \mathbf{u}_{eq} is given by

$$\mathbf{u}_{eq} = -\mathbf{f} + \ddot{\mathbf{s}}_d - \gamma \dot{\tilde{\mathbf{s}}} \quad (B6)$$

so that $\dot{\sigma} = 0$ as required. Then, the dynamics in sliding mode are

$$\ddot{\mathbf{s}} = \mathbf{f} + \mathbf{u}_{eq} = \ddot{\mathbf{s}}_d - \gamma \dot{\tilde{\mathbf{s}}} \quad (B7)$$

B.1.2 Discontinuous Control Law. The equivalent control is necessary for guiding the system on the sliding surface; however, the assumptions under which it was formed are not valid for systems with response uncertainties, like those the device must control. To address this shortcoming, the second part of designing the SMC becomes constructing a control law to drive the uncertain system response onto the sliding surface. To do this, the total control effort is decomposed into a sum of the continuous control effort \mathbf{u}_{eq} and a discontinuous, stabilizing control law \mathbf{u}_s so that the total control effort is given by

$$\mathbf{u} = \mathbf{u}_{eq} + \mathbf{u}_s \quad (B8)$$

Letting $\hat{\mathbf{f}}$ represent the uncertain system response, then the best approximation to the continuous equivalent control is

$$\hat{\mathbf{u}}_{eq} = -\hat{\mathbf{f}} + \ddot{\mathbf{s}}_d - \gamma \dot{\tilde{\mathbf{s}}} \quad (B9)$$

Then, to stabilize the system to the sliding surface, the switching logic \mathbf{u}_s is defined as

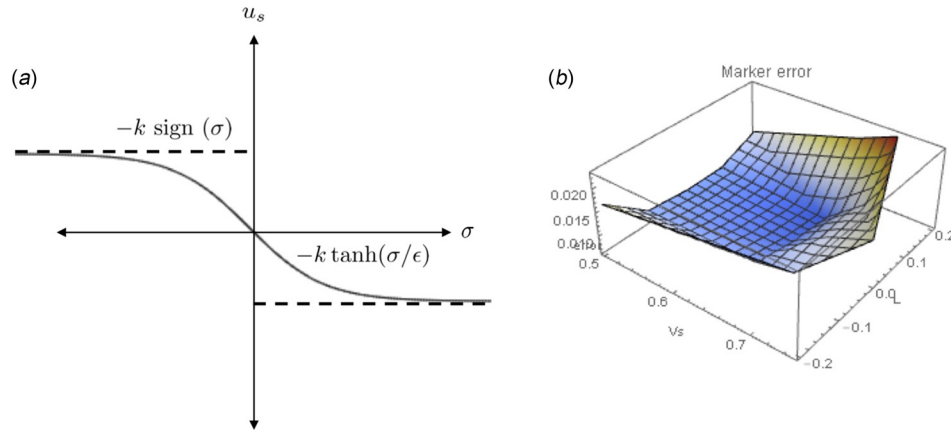


Fig. 17 (a) Discontinuous versus continuous stabilizing control laws and (b) sample tracking error plot generated by holding the value of κ constant while varying v_s and L

$$u_s = -k \text{sign}(\sigma) \quad (\text{B10})$$

where k is a constant and the $\text{sign}(\sigma)$ function is defined as

$$\text{sign}(\sigma) = \begin{cases} +1 & \text{if } \sigma > 0 \\ -1 & \text{if } \sigma < 0 \end{cases} \quad (\text{B11})$$

which makes it discontinuous across $\sigma=0$. Now, assuming that the uncertainty in the response dynamics is bounded such that

$$|f - \hat{f}| \leq F(\sigma) \quad (\text{B12})$$

k can be determined from (Eq. (B2)) through

$$\frac{1}{2} \frac{d}{dt} \sigma^2 = \dot{\sigma} \sigma = [f - \hat{f} - k \text{sign}(\sigma)] \sigma = (f - \hat{f}) \sigma - k |\sigma| \quad (\text{B13})$$

which reduces to

$$\frac{1}{2} \frac{d}{dt} \sigma^2 = F \sigma - k |\sigma| \quad (\text{B14})$$

Thus, selecting k such that

$$k = F + \eta \quad (\text{B15})$$

guarantees the conditions necessary for $\sigma=0$ to be a sliding surface (Eq. (B2)) and an invariant set [31].

B.1.3 Mitigating Chattering. The stabilizing control effort derived above represents an ideal case in which the switching between the discontinuous states of the control law can occur instantaneously and the high control activity does not excite unwanted higher frequency system dynamics. Clearly, neither of these idealizations is valid for real systems and unmodified implementations of this stabilizing control law result in unwanted system response chattering. To mitigate this chattering problem, the jump discontinuous control law $u_s = -k \text{sign}(\sigma)$ is replaced with a continuous approximation

$$u_s = -k \tanh(\sigma/\epsilon) \quad (\text{B16})$$

where ϵ is a small, strictly positive constant [32]. This continuous approximation eliminates chattering at the price of a small loss in robustness by increasing the time over which the controller switches between the two states (Fig. 17(a)). This compromise between chattering reduction and loss of robustness is necessary and acceptable in controlling mechanical systems like the ones the device is designed to manage.

Appendix C: Performance Tuning of Sliding Mode Controller

For the presented device, the relative degree of the system n is two and the state vector \mathbf{s} to be controlled is the position of the markers. Thus, after some manipulation, the control law can be written as

$$\mathbf{u} = -v_s \tanh[\kappa(\tilde{\mathbf{s}} + L\dot{\tilde{\mathbf{s}}})] \quad (\text{C1})$$

where v_s is the control effort gain, L weights the importance of marker position versus marker velocity error, and κ influences the how quickly the controller transitions between control states. Thus, tuning the controller involves selecting values for the three parameters v_s, L, κ that reduce the marker position error. While complex self-tuning methods exist to find these optimal parameters [33], a straightforward technique for determining the parameter set involves visualizing the tracking error surfaces created by varying control parameters over a range of values (Fig. 17(b)). The minimum error value on this surface plot dictates the choice of control parameter set. While this method is semimanual in nature, the tracking accuracy results achieved with this approach are sufficient for the purposes of the device.

Appendix D: Force Vector Direction Computation.

In order to compute specimen stress, the vectors along which the forces are applied $\mathbf{v}^{(ij)}$ are needed. The vectors are numbered based on specimen side and location and determination of these vectors requires a kinematic analysis of the device actuation mechanisms (Fig. 18(a)).

The procedure for finding these vectors can be illustrated through the process of finding two example vectors, $\mathbf{v}^{(1.1)}$ for the vectors attached to the bell-crank mechanisms and $\mathbf{v}^{(1.2)}$ for the center vectors. The vector $\mathbf{v}^{(1.1)}$ corresponds to the current orientation vector of the link AB (Fig. 18(b)), which can be determined from the positions of the pins A and B. The position of A can be estimated from $\mathbf{A} = \mathbf{F} \cdot \mathbf{A}_0$ where \mathbf{A}_0 is the position vector of attachment point (1.1) in the reference configuration. Likewise, the current position of point B can be calculated by

$$\mathbf{B} = \mathbf{C}_0 + \mathbf{R} \cdot [0, l_{B_0C_0}]^T \quad (\text{D1})$$

where \mathbf{C}_0 is the position of point C (fixed in space), $l_{B_0C_0}$ is the length of the link B_0C_0 , and \mathbf{R} is the rotation matrix defined as

$$\mathbf{R} = \begin{bmatrix} \cos \zeta & -\sin \zeta \\ \sin \zeta & \cos \zeta \end{bmatrix} \quad (\text{D2})$$

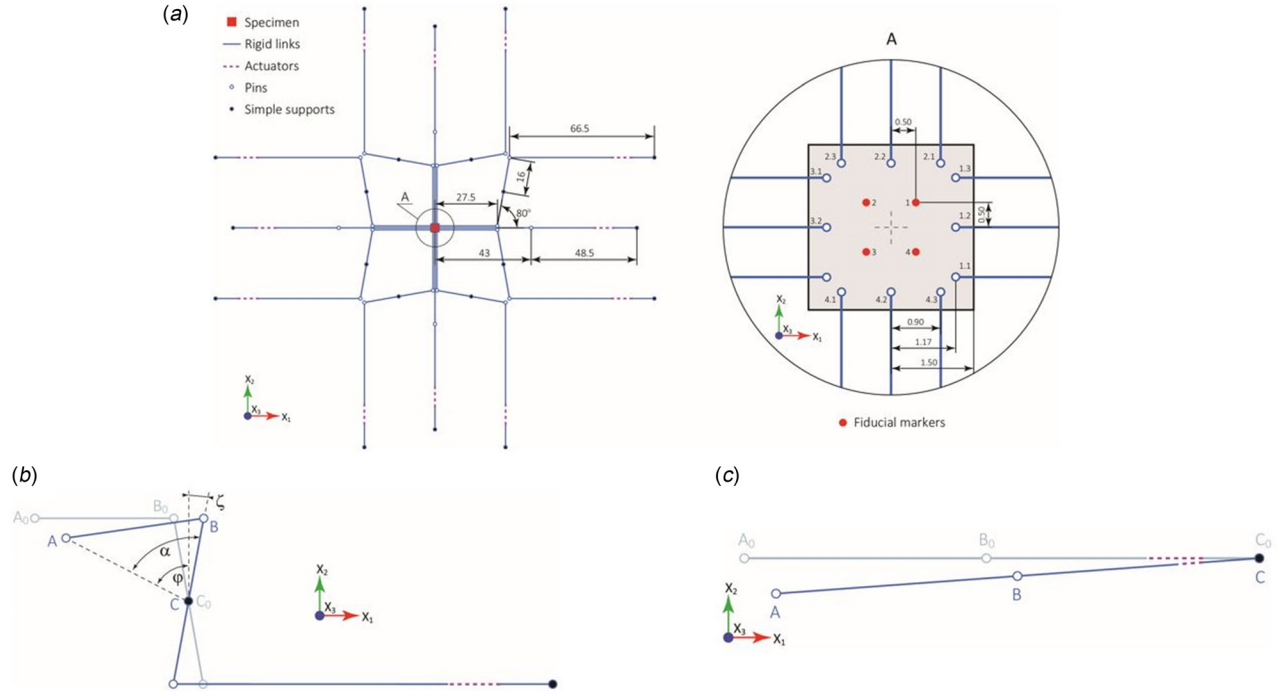


Fig. 18 (a) Actuation components of the device involved in determining the force vectors. Inset A: Numbering scheme for force vectors. (b) Geometric quantities involved in determining force vectors attached to the bell-crank attachments. (c) Geometric quantities involved in determining center force vectors.

The angle ζ is defined as

$$\begin{aligned}\zeta &= \phi - \alpha \\ \phi &= \cos^{-1} \left(\frac{\mathbf{A} - \mathbf{C}_0}{|\mathbf{A} - \mathbf{C}_0|} \cdot [0, 1] \right) \\ \alpha &= \cos^{-1} \left(\frac{l_{AC_0}^2 + l_{B_0C_0}^2 - l_{A_0B_0}^2}{2l_{AC_0}l_{B_0C_0}} \right)\end{aligned}\quad (D3)$$

where l_{AC_0} is the length of the vector between \mathbf{A} and \mathbf{C}_0 and $l_{A_0B_0}$ is the length of the link A_0B_0 . Thus, $\mathbf{v}^{(1.1)}$ is

$$\mathbf{v}^{(1.1)} = \frac{\mathbf{B} - \mathbf{A}}{|\mathbf{B} - \mathbf{A}|} \quad (D4)$$

Vector $\mathbf{v}^{(1.2)}$ can be quickly found from inspection (Fig. 18(c))

$$\mathbf{v}^{(1.2)} = \frac{\mathbf{C}_0 - \mathbf{A}}{|\mathbf{C}_0 - \mathbf{A}|} \quad (D5)$$

Appendix E: Stress Computation

The Cauchy stress tensor \mathbf{t} is calculated from the first Piola–Kirchhoff stress \mathbf{P} via $\mathbf{t} = \mathbf{P} \cdot \mathbf{F}^T$. To determine \mathbf{P} , traction vectors in the reference configuration \mathbf{T}_0 are required. \mathbf{T}_0 can be calculated from the experimentally determined forces in the deformed configuration \mathbf{f} and the reference specimen area A_0 by $\mathbf{T}_0 = \mathbf{f}/A_0$. Under generalized loading, the load cell forces on side i , $\mathbf{f}^{(i.1)}$, $\mathbf{f}^{(i.2)}$, and $\mathbf{f}^{(i.3)}$ are not equal and result in an uneven traction distribution (Fig. 19(a)). While normal stresses at the center of the specimen can be estimated from the average traction, the uneven distribution of traction must be accounted for when calculating shear stresses. When computing the stress quantities, normal traction in reference configuration is approximated with linear functions (Fig. 19(b)) and shear traction is assumed to be

evenly distributed on each side. Note, because the connection arms attached to the specimen mounting needles experience very little rotation even at large deformations, the normal traction in reference configuration will always be much greater than shear traction. Thus, the two normal traction vectors each side of the specimen are computed by

$$\begin{aligned}\mathbf{T}_{0,n}^{(1.1)} &= \frac{\beta^{(1)}}{A_0^{(1)}} \mathbf{f}^{(1.1)} \cdot \mathbf{v}_1^{(1.1)} \mathbf{T}_{0,n}^{(1.3)} = \frac{\beta^{(1)}}{A_0^{(1)}} \mathbf{f}^{(1.3)} \cdot \mathbf{v}_1^{(1.3)} \\ \mathbf{T}_{0,n}^{(2.1)} &= \frac{\beta^{(2)}}{A_0^{(2)}} \mathbf{f}^{(2.1)} \cdot \mathbf{v}_2^{(2.1)} \mathbf{T}_{0,n}^{(2.3)} = \frac{\beta^{(2)}}{A_0^{(2)}} \mathbf{f}^{(2.3)} \cdot \mathbf{v}_2^{(2.3)}\end{aligned}\quad (E1)$$

and the shear traction vector on each side by

$$\begin{aligned}\mathbf{T}_{0,s}^{(1)} &= \frac{1}{A_0^{(1)}} \left(\mathbf{f}^{(1.1)} \cdot \mathbf{v}_2^{(1.1)} + \mathbf{f}^{(1.2)} \cdot \mathbf{v}_2^{(1.2)} + \mathbf{f}^{(1.3)} \cdot \mathbf{v}_2^{(1.3)} \right) \\ \mathbf{T}_{0,s}^{(2)} &= \frac{1}{A_0^{(2)}} \left(\mathbf{f}^{(2.1)} \cdot \mathbf{v}_1^{(2.1)} + \mathbf{f}^{(2.2)} \cdot \mathbf{v}_1^{(2.2)} + \mathbf{f}^{(2.3)} \cdot \mathbf{v}_1^{(2.3)} \right)\end{aligned}\quad (E2)$$

where $\beta^{(i)}$ are scaling parameters that enforce equivalency between the linear traction distribution and the original loading state and are defined as

$$\beta^{(i)} = \frac{2 \left(\mathbf{f}^{(i.1)} \cdot \mathbf{v}_i^{(i.1)} + \mathbf{f}^{(i.2)} \cdot \mathbf{v}_i^{(i.2)} + \mathbf{f}^{(i.3)} \cdot \mathbf{v}_i^{(i.3)} \right)}{\mathbf{f}^{(i.1)} \cdot \mathbf{v}_i^{(i.1)} + \mathbf{f}^{(i.3)} \cdot \mathbf{v}_i^{(i.3)}} \quad (E3)$$

and $\mathbf{v}_k^{(ij)}$ is the vector component in the k th direction ($k \in \{1, 2\}$) of the $\mathbf{f}^{(ij)}$ force vector ($i \in \{1, 2, 3, 4\}, j \in \{1, 2, 3\}$). See Appendix D for details on calculating the force vectors.

The stress distribution inside a rectangular plate subjected to a linearly varying normal traction distribution can be estimated using the biharmonic Airy's stress function ϕ , which satisfies the differential equation

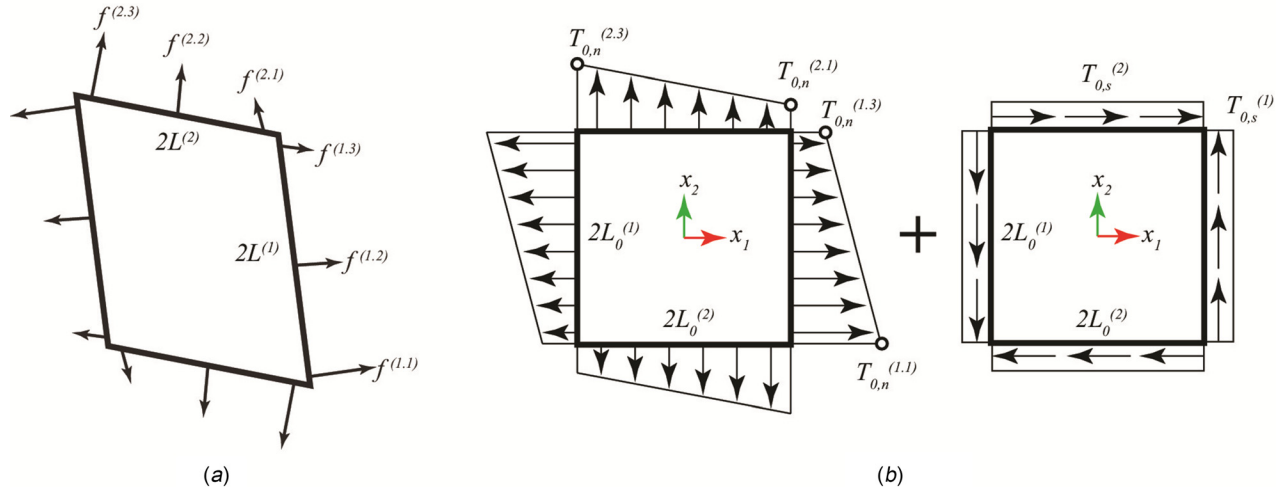


Fig. 19 (a) Force vectors in the deformed configuration and (b) resulting normal and shear traction distributions in the reference configuration

$$\nabla^4 \phi = 0 \quad (\text{E4})$$

Normal and shear stress quantities are then computed as

$$\sigma_{11} = \frac{\partial^2 \phi}{\partial x_2^2}$$

$$\sigma_{22} = \frac{\partial^2 \phi}{\partial x_1^2}$$

$$\tau_{12} = -\frac{\partial^2 \phi}{\partial x_1 \partial x_2}$$

Airy's stress function is assumed to have the form

$$\phi = ax_1^3x_2 + bx_1x_2^3 + cx_1x_2 + dx_1^2 + ex_2^2 \quad (\text{E6})$$

thus, the normal and shear stresses are

$$\sigma_{11} = 6bx_1x_2 + 2e$$

$$\sigma_{22} = 6ax_1x_2 + 2d$$

$$\tau_{12} = -3ax_1^2 - 3bx_2^2 - c$$

The coefficients a , b , c , d , and e can be found by applying the following boundary conditions:

$$x_1 = L_0^{(2)}, \quad x_2 = -L_0^{(1)}, \quad \sigma_{11} = \mathbf{T}_{0,n}^{(1,1)}$$

$$x_1 = L_0^{(2)}, \quad x_2 = L_0^{(1)}, \quad \sigma_{11} = \mathbf{T}_{0,n}^{(1,3)}$$

$$x_1 = L_0^{(2)}, \quad x_2 = L_0^{(1)}, \quad \sigma_{22} = \mathbf{T}_{0,n}^{(2,1)}$$

$$x_1 = -L_0^{(2)}, \quad x_2 = L_0^{(1)}, \quad \sigma_{22} = \mathbf{T}_{0,n}^{(2,3)}$$

$$x_1 = L_0^{(2)}, \quad x_2 = L_0^{(1)}, \quad \tau_{12} = 0 \quad (\text{E8})$$

Note, the last boundary condition is an approximation. In the case of a finite plate subjected to normal traction only, shear stresses must vanish everywhere on the boundary. The exact solution to this problem would involve infinite series.

Thus, the normal stress distributions functions are

$$\sigma_{11} = \frac{\mathbf{T}_{0,n}^{(1,3)} - \mathbf{T}_{0,n}^{(1,1)}}{2L_0^{(1)}L_0^{(2)}}x_1x_2 + \frac{\mathbf{T}_{0,n}^{(1,3)} + \mathbf{T}_{0,n}^{(1,1)}}{2} \quad (\text{E9})$$

$$\sigma_{22} = \frac{\mathbf{T}_{0,n}^{(2,1)} - \mathbf{T}_{0,n}^{(2,3)}}{2L_0^{(1)}L_0^{(2)}}x_1x_2 + \frac{\mathbf{T}_{0,n}^{(2,1)} + \mathbf{T}_{0,n}^{(2,3)}}{2}$$

(E5) and the shear stress distribution function is

$$\tau_{12} = -\frac{1}{4L_0^{(1)}L_0^{(2)}} \left[\left(\mathbf{T}_{0,n}^{(2,1)} - \mathbf{T}_{0,n}^{(2,3)} \right) \left(x_1^2 - \left(L_0^{(2)} \right)^2 \right) + \left(\mathbf{T}_{0,n}^{(1,3)} - \mathbf{T}_{0,n}^{(1,1)} \right) \left(x_2^2 - \left(L_0^{(1)} \right)^2 \right) \right] \quad (\text{E10})$$

At the center of the specimen the stress values are

$$\sigma_{11} = \frac{\mathbf{T}_{0,n}^{(1,3)} + \mathbf{T}_{0,n}^{(1,1)}}{2}$$

$$\sigma_{22} = \frac{\mathbf{T}_{0,n}^{(2,1)} + \mathbf{T}_{0,n}^{(2,3)}}{2} \quad (\text{E11})$$

$$\tau_{12} = \frac{1}{4} \left[\left(\mathbf{T}_{0,n}^{(2,1)} - \mathbf{T}_{0,n}^{(2,3)} \right) \frac{L_0^{(2)}}{L_0^{(1)}} + \left(\mathbf{T}_{0,n}^{(1,3)} - \mathbf{T}_{0,n}^{(1,1)} \right) \frac{L_0^{(1)}}{L_0^{(2)}} \right]$$

Finally, the first Piola–Kirchhoff stress tensor is

$$\mathbf{P} = \begin{bmatrix} \sigma_{11} & \tau_{12} + \mathbf{T}_{0,s}^{(2)} \\ \tau_{12} + \mathbf{T}_{0,s}^{(1)} & \sigma_{22} \end{bmatrix} \quad (\text{E12})$$

References

- [1] Fung, Y. C., 1993, *Biomechanics: Mechanical Properties of Living Tissues*, 2nd ed., Springer-Verlag, New York.
- [2] Sacks, M., 2000, "Biaxial Mechanical Evaluation of Planar Biological Materials," *J. Elasticity*, **61**, pp. 199–246.
- [3] Zhang, W., Feng, Y., Lee, C. H., Billiar, K. L., and Sacks, M. S., 2015, "A Generalized Method for the Analysis of Planar Biaxial Mechanical Data Using Tethered Testing Configurations," *ASME J. Biomech. Eng.*, **137**(6), p. 064501.
- [4] Grashow, J. S., Yoganathan, A. P., and Sacks, M. S., 2006, "Biaxial Stress-Stretch Behavior of the Mitral Valve Anterior Leaflet at Physiologic Strain Rates," *Ann. Biomed. Eng.*, **34**(2), pp. 315–325.

- [5] Sacks, M. S., 1999, "A Method for Planar Biaxial Mechanical Testing That Includes In-Plane Shear," *ASME J. Biomech. Eng.*, **121**(5), pp. 551–555.
- [6] Raghupathy, R., and Barocas, V. H., 2010, "Generalized Anisotropic Inverse Mechanics for Soft Tissues," *ASME J. Biomech. Eng.*, **132**(8), p. 081006.
- [7] Aggarwal, A., and Sacks, M. S., 2015, "An Inverse Modeling Approach for Semilunar Heart Valve Leaflet Mechanics: Exploitation of Tissue Structure," *Biomech. Model. Mechanobiol.*, **15**(4), pp. 1–24.
- [8] Lee, C. H., Amini, R., Gorman, R. C., Gorman, J. H., 3rd., and Sacks, M. S., 2014, "An Inverse Modeling Approach for Stress Estimation in Mitral Valve Anterior Leaflet Valvuloplasty for In-Vivo Valvular Biomaterial Assessment," *J. Biomech.*, **47**(9), pp. 2055–2063.
- [9] Ferruzzi, J., Bersi, M. R., and Humphrey, J. D., 2013, "Biomechanical Phenotyping of Central Arteries in Health and Disease: Advantages of and Methods for Murine Models," *Ann. Biomed. Eng.*, **41**(7), pp. 1311–1330.
- [10] Billiar, K. L., and Sacks, M. S., 1997, "A Method to Quantify the Fiber Kinematics of Planar Tissues Under Biaxial Stretch," *J. Biomech.*, **30**(7), pp. 753–756.
- [11] Nielsen, P. M., Hunter, P. J., and Smaill, B. H., 1991, "Biaxial Testing of Membrane Biomaterials: Testing Equipment and Procedures," *ASME J. Biomech. Eng.*, **113**(3), pp. 295–300.
- [12] Sun, W., Sacks, M. S., and Scott, M. J., 2005, "Effects of Boundary Conditions on the Estimation of the Planar Biaxial Mechanical Properties of Soft Tissues," *ASME J. Biomech. Eng.*, **127**(4), pp. 709–715.
- [13] Rivlin, R. S., and Saunders, D. W., 1951, "Large Elastic Deformations of Isotropic Materials—7: Experiments on the Deformation of Rubber," *Philos. Trans. R. Soc. London Ser. A*, **243**(865), pp. 251–288.
- [14] Billiar, K. L., and Sacks, M. S., 2000, "Biaxial Mechanical Properties of the Natural and Glutaraldehyde Treated Aortic Valve Cusp—Part I: Experimental Results," *ASME J. Biomech. Eng.*, **122**(1), pp. 23–30.
- [15] Eilaghi, A., Flanagan, J. G., Brodland, G. W., and Ethier, C. R., 2009, "Strain Uniformity in Biaxial Specimens Is Highly Sensitive to Attachment Details," *ASME J. Biomech. Eng.*, **131**(9), p. 091003.
- [16] Jacobs, N. T., Cortes, D. H., Vresilovic, E. J., and Elliott, D. M., 2013, "Biaxial Tension of Fibrous Tissue: Using Finite Element Methods to Address Experimental Challenges Arising From Boundary Conditions and Anisotropy," *ASME J. Biomech. Eng.*, **135**(2), p. 021004.
- [17] Utkin, V., 1977, "Variable Structure Systems With Sliding Modes," *IEEE Trans. Autom. Control*, **22**(2), pp. 212–222.
- [18] DeCarlo, R., Zak, S., and Matthews, G., 1988, "Variable Structure Control of Nonlinear Multivariable Systems: A Tutorial," *Proc. IEEE*, **76**(3), pp. 212–232.
- [19] Fan, R., and Sacks, M. S., 2014, "Simulation of Planar Soft Tissues Using a Structural Constitutive Model: Finite Element Implementation and Validation," *J. Biomech.*, **47**(9), pp. 2043–2054.
- [20] Sacks, M. S., and Chuong, C. J., 1998, "Orthotropic Mechanical Properties of Chemically Treated Bovine Pericardium," *Ann. Biomed. Eng.*, **26**(5), pp. 892–902.
- [21] Collins, M., Eberth, J. F., Wilson, E., and Humphrey, J., 2012, "Acute Mechanical Effects of Elastase on the Infrarenal Mouse Aorta: Implications for Models of Aneurysms," *J. Biomech.*, **45**(4), pp. 660–665.
- [22] Eberth, J. F., Popovic, N., Gresham, V. C., Wilson, E., and Humphrey, J. D., 2010, "Time Course of Carotid Artery Growth and Remodeling in Response to Altered Pulsatility," *Am. J. Physiol. Heart Circ. Physiol.*, **299**(6), pp. H1875–H1883.
- [23] Chen, K., Fata, B., and Einstein, D. R., 2008, "Characterization of the Highly Nonlinear and Anisotropic Vascular Tissues From Experimental Inflation Data: A Validation Study Toward the Use of Clinical Data for In-Vivo Modeling and Analysis," *Ann. Biomed. Eng.*, **36**(10), pp. 1668–1680.
- [24] Rausch, M. K., Famaey, N., Shultz, T. O., Bothe, W., Miller, D. C., and Kuhl, E., 2013, "Mechanics of the Mitral Valve: A Critical Review, an In Vivo Parameter Identification, and the Effect of Prestrain," *Biomech. Model. Mechanobiol.*, **12**(5), pp. 1053–1071.
- [25] Billiar, K. L., and Sacks, M. S., 2000, "Biaxial Mechanical Properties of the Native and Glutaraldehyde-Treated Aortic Valve Cusp—Part II: A Structural Constitutive Model," *ASME J. Biomech. Eng.*, **122**(4), pp. 327–335.
- [26] Humphrey, J. D., Strumpf, R. K., and Yin, F. C., 1990, "Determination of a Constitutive Relation for Passive Myocardium—I: A New Functional Form," *ASME J. Biomech. Eng.*, **112**(3), pp. 333–339.
- [27] Humphrey, J. D., Strumpf, R. K., and Yin, F. C., 1990, "Determination of a Constitutive Relation for Passive Myocardium—II: Parameter Estimation," *ASME J. Biomech. Eng.*, **112**(3), pp. 340–346.
- [28] Lee, C. H., Feaver, K., Zhang, W., Gorman, R. C., Gorman, J. H., and Sacks, M. S., 2016, "Inverse Modeling Based Estimation of In-Vivo Stresses and Their Relation to Simulated Layer-Specific Interstitial Cell Deformations in the Mitral Valve," Summer Biomechanics, Bioengineering and Biotransport Conference (SB3C), National Harbor, MD, June 29–July 2.
- [29] Wagenseil, J. E., Nerurkar, N. L., Knutsen, R. H., Okamoto, R. J., Li, D. Y., and Mecham, R. P., 2005, "Effects of Elastin Haploinsufficiency on the Mechanical Behavior of Mouse Arteries," *Am. J. Physiol. Heart Circ. Physiol.*, **289**(3), pp. 1209–1217.
- [30] Chai, S., Chai, Q., Danielsen, C. C., Hjorth, P., Nyengaard, J. R., Ledet, T., Yamaguchi, Y., Rasmussen, L. M., and Wogensen, L., 2005, "Overexpression of Hyaluronan in the Tunica Media Promotes the Development of Atherosclerosis," *Circ. Res.*, **96**(5), pp. 583–591.
- [31] Slotine, J.-J. E., and Li, W., 1991, *Applied Nonlinear Control*, Prentice Hall, Englewood Cliffs, NJ.
- [32] Edwards, C., and Spurgeon, S., 1998, *Sliding Mode Control: Theory and Applications*, CRC Press, Boca Raton, FL.
- [33] Kuo, T.-C., Huang, Y.-J., and Chang, S.-H., 2008, "Sliding Mode Control With Self-Tuning Law for Uncertain Nonlinear Systems," *ISA Trans.*, **47**(2), pp. 171–178.